Multitemporal analysis of Sentinel-1 ~~backscattering~~ backscatter during snow melt using high-resolution field measurements and radiative transfer ~~modeling~~modelling

Francesca Carletti[1,2], Carlo Marin[3], Chiara Ghielmini[1], Mathias Bavay[1], and Michael Lehning[1,2]

[1]WSL Institute for Snow and Avalanche Research SLF, Davos, Switzerland
[2]School of Architecture, Civil and Environmental Engineering, École Polytechnique Fédérale de Lausanne EPFL, Lausanne, Switzerland
[3]Institute for Earth Observation, Eurac Research, Bolzano, Italy

Correspondence: Francesca Carletti (francesca.carletti@slf.ch)

Abstract. The spatiotemporal evolution of snow melt is fundamental for water resources management and risk mitigation in mountain catchments. Synthetic Aperture Radar (SAR) images acquired by satellite systems such as Sentinel-1 (S1) are promising for monitoring wet snow due to their high sensitivity to liquid water content (LWC) and ability to provide spatially distributed data at a high temporal ~~resolutions~~resolution. While recent studies have ~~successfully linked~~ linked multitemporal S1 backscattering to ~~various phasesof snowpack melting~~snow melt phases, a correlation with detailed snowpack properties is still missing. To address this, we collected the first dataset of ~~detailed~~ comprehensive wet snow properties tailored for SAR applications over two consecutive snow seasons at the Weissfluhjoch field site ~~in~~ near Davos, Switzerland. First, ~~our dataset enabled the validation of previous methods relying on multitemporal SAR~~ we tested previous methods which use multitemporal S1 backscattering to characterize melting ~~snowpacks and physically linked the~~ phases, and demonstrated that the observed monotonous increase in backscattering following the local minimum ~~to the evolution~~ is due to the development of surface roughness. Then, ~~the dataset was used~~ we used the measured snow properties as input to the Snow Microwave Radiative Transfer (SMRT) model to reproduce ~~the~~ S1 backscattering ~~signal~~signals. Our simulations showed ~~a general negative bias compared to the satellite data, with the most significant drivers being LWC~~that rather than melting phases, time series of backscattering rather identify regimes dominated by either LWC, early in the ~~melt seasonand the surface roughness~~season, or surface roughness, later on. The results also highlight several key challenges for reconciling S1 signals with radiative transfer simulations of wet snow: (i) the discrepancy in spatiotemporal variability of LWC as seen by the satellite and validation measurements, (ii) the lack of fully validated permittivity, microstructure and roughness models for wet snow in the C-band, (iii) the difficulty of capturing wet snow features potentially generating stronger scattering effects on a large scale ~~,~~ – such as internal snowpack structures, soil features in case of low LWC, and surface roughness ~~,~~ – which are not necessarily captured by point-wise measurements.

1 Introduction

Seasonal snowpack in mountain catchments is one of the most important water resources, as it accumulates and stores water during winter and releases it consistently in the form of runoff during the melting period (Viviroli and Weingartner, 2004). In ~~fact, discharge in Alpine streams~~ alpine streams, discharge is largely dominated by snow melt from May to July and more than one sixth of the world's population relies on meltwater released from higher altitudes for drinking water, crop irrigation and hydropower production (Beniston et al., 2018). However, ~~this~~ melting snow can also cause wet- and glide-snow avalanches (Bellaire et al., 2017; Fromm et al., 2018), which pose significant threats to human life and infrastructures. Additionally, rain-on-snow events on ~~snowpacks with high liquid water content~~ already wet snowpacks are linked to increased runoff and shorter time lags between ~~the onset of the event~~ precipitation onset and the resulting runoff (Würzer et al., 2016). These events can have catastrophic consequences and their occurrence is supposed to increase ~~as a first response to~~ in response to a sustained warming (Beniston and Stoffel, 2016). Therefore, information about the spatiotemporal evolution of snow melt is beneficial for both the management of water resources and for risk mitigation.

Identifying wet snow is complex both when using manual measurements, automatic instruments and ~~physically based~~ physics-based snow models. Datasets of manual measurements of snow water equivalent (SWE) and liquid water content (LWC hereafter) at high temporal resolution are generally rare due to the ~~required amount of work and resources to collect them~~time, effort and resources required for their collection. There have been considerable advances in ~~the development of technologies that exploit~~ technologies that use the dielectric properties of snow in the microwave range to estimate LWC in a non-destructive way (Schmid et al., 2014; Koch et al., 2014). However, the application of these methods is limited to one single point without the possibility to capture the spatial variability of the processes. Additionally, their installation and maintenance is often complicated and expensive, and the extraction of the physical parameters is usually hindered by noise. ~~Physically based~~ physics-based layered snow models like the SNOWPACK-Alpine3D model chain (Bartelt and Lehning, 2002; Lehning et al., 2006) or GEOtop (Endrizzi et al., 2014) are used to overcome these challenges, as they can simulate LWC and SWE at high spatial and temporal resolutions ~~only~~ based on meteorological forcings. However, meteorological forcings also represent a major source of uncertainty ~~- -~~ especially when needed at high spatial resolution ~~- -~~ affecting the accuracy of the results (Raleigh et al., 2015)~~, together with the uncertainty~~ . This adds up to the uncertainties related to the amount and type of ~~used parametrizations~~ parametrizations used (Günther et al., 2019).

In this context, a valuable opportunity to identify wet snow is offered by synthetic aperture radar (SAR hereafter) systems. SAR measurements are highly sensitive to the free liquid water contained in wet snow (Nagler and Rott, 2000). At certain frequencies, the increase in liquid water generates high dielectric losses and increased absorption coefficients (Denoth et al., 1984; Sihvola and Tiuri, 1986; Mätzler, 1987; Ulaby et al., 2014). Therefore, the radar ~~backscattering~~ backscatter drops to lower intensities with respect to winter averages ~~(Ulaby et al., 1987, 2014; Nagler and Rott, 2000; Nagler et al., 2016; Lin et al., 2016). Basing on this principle, multitemporal SAR data~~ (Ulaby et al., 1987; Strozzi et al., 1997; Strozzi and Matzler, 1998; Nagler and Rott, 200 . This raised the question of whether different types of snow cover could be classified based on their response to active microwave signals. This challenge has been addressed with various approaches over the years. Between 1993 and 1995,

at the field site of Weissfluhjoch in the Swiss Alps, Strozzi et al. (1997); Strozzi and Matzler (1998) conducted tower-based C-band radiometric measurements at all polarizations across a wide range of incidence angles. Simultaneously, they carried out monthly measurements of snow physical properties. These measurements were used to ~~develop algorithms for the generation of wet-snow maps (Nagler and Rott, 2000; Nagler et al., 2016). There have been further efforts in developing algorithms to derive LWC using C-band full-polarimetric SAR images (Shi et al., 1993; Shi and Dozier, 1995). However, Strozzi et al. (1997); Kendra et al. (19~~ ~~expressed their doubts about the theoretical background and the~~ classify the observed snow covers into categories ranging from dry snowpacks, to thin moist layers overlying dry snow, to wet snowpacks with either smooth or rough surfaces. Relying on a tower-based radiometer, the experiments were highly controlled, allowing detailed investigation of radar responses to each snow condition. Nevertheless, significant sources of uncertainty remained – especially the influence of surface roughness on wet snow surfaces, which was not quantitatively measured, but only qualitatively assessed. These detailed studies, along with the work of Kendra et al. (1998), raised questions about theoretical foundations and systematic reliability of ~~these algorithms . With tower-based experiments on wet snow, they found that the backscattering behavior used for the retrieval algorithms might~~ LWC retrieval algorithms based on C-band full-polarimetric SAR imagery, which had been developed shortly before (Shi et al., 1993; Shi and Dozier, 1995). In particular, the scattering mechanisms assumed in these retrievals may have been biased by a combination of conditions ~~leading to a strong prevalence of surface scattering mechanisms~~that strongly favored surface scattering. Extending the prior knowledge to a spatial and multitemporal context, (Nagler and Rott, 2000) developed an algorithm based on repeat-pass SAR images to map wet-snow in mountainous areas, defining a backscatter drop of 3 dB to distinguish wet snow from other surfaces. Comparisons with snow maps from different sources showed generally good agreement above the snow line, but consistent biases in areas with fragmented snow cover.

After a progress freeze due to the ~~lack~~ scarcity of SAR data in the past and simultaneous ~~ground truth measurements, there was a renewed~~ field measurements, the research interest in the ~~use of radar waves to track snow melting processes~~ topic was renewed since the launch of the Sentinel-1 (S1 hereafter) joint mission of the European Space Agency (ESA) and the European Commission in 2014. At ~~Alpine~~ alpine latitudes, S1 acquires C-band SAR imagery in the early morning and late afternoon, regardless of the weather, with a revisit time of 6 days. The SAR imagery is available free of charge. Marin et al. (2020) used these images for the first time to develop a correlation between the multitemporal S1 SAR ~~backscattering and the snowmelt~~ backscatter and the snow melt dynamics. Over 5 different ~~Alpine~~ alpine sites, the authors have found that the multitemporal S1 SAR acquisitions allow the detection of the melting phases, i.e. moistening, ripening and runoff (Dingman, 2015) with a good agreement with in-situ observations and layered, ~~physically-based~~ physics-based snow models. In particular, the ~~backscattering~~ backscatter decreased as soon as liquid water appeared in the snowpack and increased progressively and simultaneously with the runoff release. Deriving and applying a set of identification rules, the authors could define the melting phases for the test sites with relatively small lag errors with respect to the revisit time of S1. Consequently, local minima in S1 multitemporal backscatter time series and sharp increases thereafter were associated with snowpack saturation, the onset of runoff, and snow ablation (Darychuk et al., 2023; Gagliano et al., 2023).

~~This approach holds~~ These approaches hold great potential for monitoring the temporal evolution of the melting dynamics, ~~especially~~ particularly over wide and scarcely instrumented areas. However, ~~in order to fully understand the potential~~

of to fully use the multitemporal information made available from provided by S1 for snowmelt snow melt monitoring, a deeper understanding of the scattering mechanisms of melting snow is needed. In particularunderlying scattering mechanisms – especially the role of surface roughness (Marin et al., 2020) – is still required. Specifically, knowing the time window in which different scattering effects dominate and under which conditions the the C-band radar backscattering backscatter is fully absorbed by the melting snowpack would enable to extract as much information as possible from S1 multitemporal backscattering. Up-to-datetime series. To date, the only effort in this direction has been done by Brangers et al. (2024) by means of was made by Brangers et al. (2024) using tower-based C-band measurements, which, however, lack . However, this study lacks high-temporal-resolution ground-truth validation at high temporal resolution with measured snow properties. Additionally, the snowpack melt-out has been often associated with sharp increases in backscattering following the local minima (Marin et al., 2020; Darychuk et al., 2023; Gagliano et al., 2023). However, the underlying physical processes that determine this trend, among which the effect of surface roughness (Marin et al., 2020), remain to be investigatedMoreover, comparisons with S1 were hindered by several factors, including sensor calibration issues and the small footprint size – which likely introduced speckle noise and failed capturing larger-scale scattering processes.

The main limitation that has hindered Overall, the main limitation to improving the understanding of SAR mechanisms the interaction of S1 backscatter signals with melting snow cover is the lack of reference ground data, especially during the melting season. Over Alpine . Over alpine snowpacks, it is not uncommon common to observe the formation of ice layers either at the surface (Quéno et al., 2018) or at deeper snowpack depths (Pfeffer and Humphrey, 1998). Moreover, in temperate Alpine alpine areas characterized by high snow accumulation and intense solar radiation, suncups may form spontaneously on the snow surface during the ablation season (Post and LaChapelle, 2000; Mitchell and Tiedje, 2010), increasing the surface roughness significantly (Fassnacht et al., 2009). These phenomena are known to impact the radar response to wet snow (Kendra et al., 1998; Yueh et al., 2009; Nagler and Rott, 2000; Shi and Dozier, 1995)(Shi and Dozier, 1995; Strozzi and Matzler, 1998; K
.

A promising path to explore the interaction between C-band active microwaves and scattering properties of wet snow surfaces is through However, high-resolution and detailed snow measurements alone are insufficient to address this issue. It is equally important to rely on a method to interpret them from a radar perspective. A promising and increasingly adopted approach involves the use of state-of-the-art radiative transfer (RT hereafter) models. Picard et al. (2018) developed the Snow Microwave Radiative Transfer (SMRT) model, a versatile model that can be used in active and passive mode to compute backscattering backscatter and brightness temperature from multilayered media such as snowpacks or ice sheets overlying reflective surfaces, e.g. ground, ice, or water. SMRT responds to the need of a modular and flexible approach to unify and compare the wide range of pre-existing representations of microstructure, electromagnetic theories, soil models and permittivity formulations. While wet snow holds significant importance for various applications, both SMRT and other similar models have primarily been were primarily developed and validated under for dry snow conditions in Arctic and Antarctic snowpacks, or ice sheets (Proksch et al., 2015; Rott et al., 2021; Soriot et al., 2022; Meloche et al., 2022; Husman et al., 2023). Both the vertical structure and the surface of these types of snowpack are often less complex than that of a seasonal Alpine alpine snowpack. To date, the above mentioned ensemble of complex melting snowpack processes has been scarcely investigated by means of radiative transfer

models due to the lack of ground reference data (Shi and Dozier, 1995; Strozzi et al., 1997; Kendra et al., 1998; Nagler and Rott, 2000; Magagi and Bernier, 2003; Lodigiani et al., 2025). Murfitt et al. (2024) recently used SMRT to explore, for the first time, the temporal evolution of the interaction between wet snow and radar waves in a study on lake ice melt. However, the radiative transfer ~~modeling~~ modelling of wet snow still lacks dedicated effort and validation.

~~This work aims at collecting~~ The objective of this work is to collect the first ground reference dataset on melting snow tailored for SAR applications and to ~~verify the ability of a current, state-of-the-art RT model (SMRT) to reproduce the backscattering signal~~ use it together with SMRT to better understand the key processes governing the backscatter signatures recorded by S1. Previously, only Lund et al. (2022) carried out ~~an~~ a similarly extensive snow pit campaign in coordination with S1 passages. ~~Their work facilitated~~ While this study helped advance the interpretation of S1 ~~backscattering response~~ backscatter responses to diurnal snowpack ~~features. However~~variations, important scattering properties such as the optical diameter and the surface roughness were not ~~sampled and their effect on the backscattering was not explored through radiative transfer modeling. In this~~ measured. As a result, interpreting these measurements from the radar perspective – and consequently comparing them with S1 acquisitions – was not possible. In our work, we focus on the co-polarized vertical backscattering only, due to its high signal to noise ratio for wet snow (Naderpour et al., 2022) and to the fact that, due to the partial implementation of some of the key processes, it is not possible to simulate accurate cross-polarized backscattering responses with the current version of SMRT. To our knowledge, this is the first attempt to ~~use SMRT and ground measurements~~ translate ground measurements – specifically designed for RT ~~modeling –~~ modelling, including wetness and roughness – ~~to reproduce~~ into radar signals using SMRT to reproduce and interpret S1 ~~backscattering~~ acquisitions over a wet, multilayered ~~Alpine~~ alpine snowpack. This research ~~will allow us to derive several important information on RT modelling of wet snow, namely the influence of the spatial and temporal variability of liquid water content~~ provides valuable insights in two main areas. First, it advances the understanding of the interaction between S1 radar backscatter and wet snow. Specifically, it reveals the effects of spatiotemporal variability of LWC within the S1 ~~cell~~ footprint occurring between satellite ~~acquisitions and in situ measurements, the influence~~ and measurement acquisitions. It also describes the impact of surface roughness ~~, the lack of fully validated models of permittivity and roughness for wet snow at the C-band and the difficulty of~~ on backscatter signatures and highlights challenges in capturing key wet snow conditions ~~generating scattering , namely~~ that likely generate scattering at wider-scales. These include internal snowpack structures, large-scale surface roughness, and interactions with the wet soil interface when the snowpack is only slightly wet. Second, the study addresses the RT modelling of melting, layered snowpacks, highlighting the current lack of fully validated permittivity and roughness models for wet snow at C-band frequencies. With ground reference data and adequate process understanding and ~~modeling~~modelling, RT models like SMRT may evolve in tools to interpret and translate the information contained in multitemporal SAR ~~backscattering signals~~ backscatter into valuable input for ~~snow modeling~~snow-hydrological modelling.

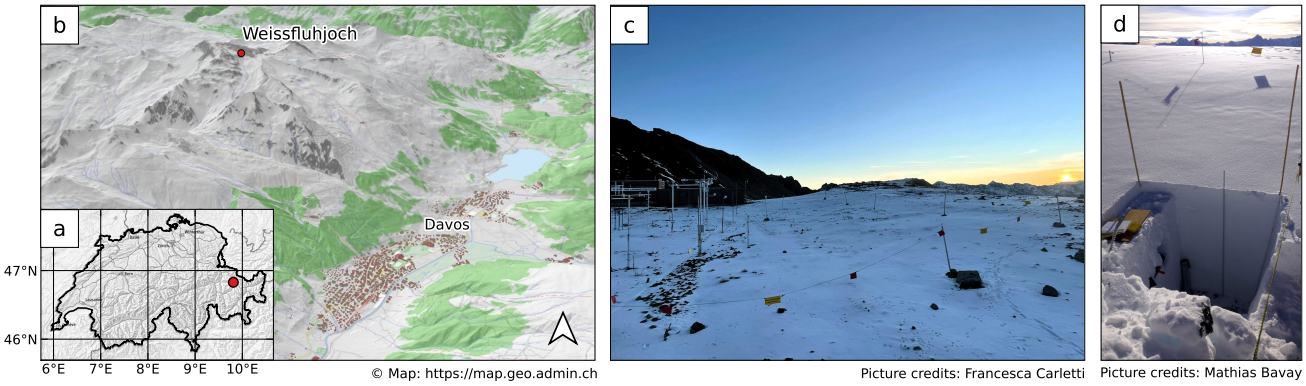

Figure 1. Location of the Weissfluhjoch field site with respect to Swiss national borders (a) and the ~~area~~ town of Davos (b). The designated area ~~dedicated to the~~ for snow profiles is shown in (c) under semi-snow-free conditions (picture taken in Sep 2024, camera oriented towards the north-east), ~~delimited~~ enclosed by ~~the~~ a flagged fence~~, camera facing north-east~~. ~~Only~~ It is worth noting that only a ~~fraction of the length~~ portion of ~~the~~ this fenced area was effectively used for snow profiles. Picture (d) shows the typical snowpit measurement ~~setting~~setup.

2 Campaign overview

This work builds upon a dataset ~~composed~~ of 85 snow pits collected ~~within a measurement campaign which took place over the two consecutive snow seasons of~~ during a two-season campaign (2022-2023 and 2023-2024) at the high-altitude ~~field site of~~ Weissfluhjoch Versuchsfeld (WFJ) field site, located in the Rhaetian Alps ~~in the Davosarea, canton of Grisons~~near Davos, Switzerland. The measurement field lies at an altitude of 2536 m a.s.l. on a relatively flat area embedded in a ~~valley facing~~ south-east facing valley. The site is partially wind sheltered from a small hill situated on the south-east ~~, however~~ – however, the dominant wind blows from north-west, in addition to katabatic wind. For this measurement campaign, we secured a protected field covering approximately ~~the same~~ two times the footprint area of S1, i.e. 20 × 20 m~~next to the officially delimited field~~. However, only a ~~fraction~~ portion of this field was effectively used for measurements~~. This designated area~~ , while the remaining area was consistently left undisturbed. The secured field has a light slope value between 2 and 7%. The flatness of the terrain is fundamental for the study of the interaction between wet snow and the C-band co-polarized vertical ~~backscattering~~ backscatter signal (σ_0^{VV} hereafter). On the one hand, σ_0^{VV} is less sensitive to changes in snow wetness ~~in areas of steep topographies~~ at low incidence angles (Nagler et al., 2016); on the other hand, ~~steep slopes cause~~ on steep slopes, the liquid water ~~to redistribute~~ redistributes laterally, at least partially (Wever et al., 2016). The field site of WFJ is equipped with advanced meteorological sensors recording meteorological forcings at sub-hourly resolutions, and moreover, with first snow observations dating back to 1936, it holds one of the longest recorded time series of snow measurements for a high-altitude research station (Marty and Meister, 2012). The site is ideal for intensive measurement campaigns, as it is easily accessible, protected from avalanche danger and the two huts provide shelter, storage space for instruments, power and internet connection.

The objective of the measurement campaign was to build a dataset ~~that would provide~~ of ground-truth reference for the interpretation of S1 σ_0^{VV} to monitor snow melt processes. Therefore, the ~~campaign~~ measurements targeted the main scattering

properties of snow: temperature, density, specific surface area (SSA), liquid water content (LWC) and surface roughness. These properties needed to be measured at a high vertical and temporal resolution to track the progression of the wetting front within the snowpack, and possibly in concomitance with S1 acquisitions. Additionally, we measured snow water equivalent (SWE), a key variable for snow melt monitoring. The resulting dataset is a time series of manually measured snow profiles describing the evolution of snow scattering properties at ~~an~~ unprecedented vertical and temporal ~~resolution~~resolutions. The dataset consists of 38 snow profiles for the season of 2022-2023 (starting in February and ending in June) and 47 for the season of 2023-2024 (starting in November and ending in July). In dry snow conditions, measurements were carried out once per week. On the first season, once the snowpack reached the full isothermal state, measurements have been carried out regularly every second working day for a total of three times per week. On the following season, the regularity of the measurements was partially given up in ~~favour~~ favor of a better synchronization with S1 acquisitions. To get the fullest possible picture to interpret the melt dynamics, manual measurements are accompanied by automatically recorded time series of runoff and SWE.

2.1 Manual measurements

2.1.1 Temperature

Snow temperature serves to monitor the progression of the snowpack to the ~~(partial)~~ isothermal state, which allows the presence of liquid water. Profiles of snow temperature were sampled from the surface to the bottom with a vertical resolution of 10 cm on snow season 2022-2023 and of 5 cm on snow season 2023-2024 using a batch of HI98501 Checktemp from Hanna (HannaInstrumentsInc.). According to the instrument specifications, the uncertainty range is $\pm$ 0.2°C. Each temperature reading was marked down after waiting an adequate time for measurement stabilization.

2.1.2 Density

In dry snow conditions, snow density controls (i) the probability of scattering events, as denser snow has more grains per unit volume and (ii) the real part of the effective permittivity (see the following Sec. 3.2), which increases with the increased fraction of ice relative to air, typical of denser snow. Profiles of snow density were sampled from the surface to the bottom with a vertical resolution of 3 cm using a box density cutter and a digital scale. The box cutter used for this campaign has a volume of 100 cm^3. The uncertainty range of this instrument is between 5 and 10% with the main ~~uncertainty sources being caused by~~ sources being the presence of ice layers, the compaction of light snow while collecting the sample, or losing fractions of ~~the sample~~ it in conditions of fragile snow such as facets or depth hoar (Conger and McClung, 2009; Proksch et al., 2016).

2.1.3 Specific Surface Area

~~Profiles of snow~~ Snow specific surface area (SSA) expresses the surface area of snow grains per unit mass, and is related to the grain size and structure. Smaller grains give higher values of SSA – meaning that the number of scattering centers is increased, but the effect of each one is weakened. Therefore, when grains are too small, the total backscatter can decrease. Larger grains, on the other hand, give lower values of SSA – meaning that scatterers are fewer but stronger and more efficient. Therefore, with

enhanced volume scattering, the overall backscatter increases. Profiles of SSA were sampled from the surface to the bottom with a vertical resolution of 4 cm using the InfraSnow sensor from FPGA (FPGA Company; Wolfsperger et al., 2022). This non-destructive method builds upon the principle of diffuse near-infrared reflectance measurements using a compact integrating sphere setup to derive optical equivalent grain diameter (OED), and therefore SSA (Gergely et al., 2014). To compute OED, snow density is required as an input parameter and for this we use the measured density profile. With a relative error of $RMSE = 15\%$ (Wolfsperger et al., 2022) when compared to μ-CT, this instrument seems to be slightly less accurate than others commonly used such as the IceCube (Zuanon, 2013), however, this bias is more pronounced for high values of SSA typical of dry snow, which is not the main object of our study. Moreover, the use of the InfraSnow is especially practical and portable for field applications.

2.1.4 Liquid Water Content

~~Profiles of snow~~ The formation of liquid water content (LWC) in the snowpack enhances its dielectric constant, leading to higher absorption losses and significant reduction in radar penetration depth. These concepts will be addressed in more detail in Sec. 3.2. Profiles of LWC were sampled from the surface to the bottom with a vertical resolution of 2, 5 or 10 cm, depending on the method. We used dielectric sensors coupled with melting calorimetry to corroborate measurements in conditions of high LWC at later stages of the melting process. To our knowledge, this is the first time series of ~~liquid water content~~ LWC snow profiles measured at such high vertical and temporal resolution. On the first campaign year, we used the Denoth capacitive sensor (Denoth, 1994) ("Denothmeter" hereafter). It consists of a flat capacitance probe with an estimated measurement surface of 176 cm^2 (Techel and Pielmeier, 2011). The probe operates at a frequency of 20 MHz and measures the real part of the permittivity of snow, and a separate measurement of density is required to obtain the imaginary part (Denoth et al., 1984; Denoth, 1989) – here, similarly than for SSA, we used the measured density profile. The Denothmeter has been widely used in field studies to monitor the evolution of snowpack wetness (Fierz and Föhn, 1994; Kattelmann and Dozier, 1999; Techel and Pielmeier, 2011), alone or in comparison with other techniques, e.g. in Koch et al. (2014); Wolfsperger et al. (2023); Barella et al. (2024). On the second campaign year, we adopted the new capacitive snow sensor (NCS hereafter) developed at the Institute for Snow and Avalanche Research SLF (Wolfsperger et al., 2023) and produced in batch series from FPGA company. The use of the Denothmeter was discontinued because it is not commercially available, and only two units were available to us, risking measurement continuity if damaged during intensive use. The NCS works in the same way as the Denothmeter, operates at the same frequency and measures over a slightly larger surface of 202 cm^2. The NCS was compared against the Denothmeter in both field and ~~lab~~ laboratory settings and the agreement was generally good, however, in ~~some~~ isolated cases of very wet layers~~(Fierz, 2009)~~, the measured permittivity tended to deviate towards higher values (Wolfsperger et al., 2023). A good element of consistency is that the comparison between ~~the NCS and the~~ NCS and Denothmeter was carried out within this campaign, in the snow season 2022-2023. The absolute error associated with dielectric measurements was estimated around 1% in volume (Sihvola and Tiuri, 1986; Fierz and Föhn, 1994). To our knowledge, a systematic study on the errors associated with the Denothmeter was never carried out. However, similar studies are available for the Finnish snow fork (Sihvola and Tiuri, 1986), which directly measures both real and imaginary parts of snow permittivity. The error associated to the snow fork

in measuring LWC is between ±0.5% (Sihvola and Tiuri, 1986) and ±0.3% (Moldestad, 2005). (Techel and Pielmeier, 2011) used both the Denothmeter and the Snow Fork in their study, reporting differences of around 1% between the two instruments. Additional uncertainties for dielectric measurements derive from interference with solar radiation near the surface (Lundberg, 2008), which we tried to minimize throughout the campaign.

Because dielectric devices may lose accuracy for high LWC values (Perla and Banner, 1988; Techel and Pielmeier, 2011), for both snow seasons, in conditions of ripe snow, ~~measurements with~~ Denothmeter/NCS measurements were backed up with melting calorimetry following the revised field protocol recently described in Barella et al. (2024) and partially carried out within the same measurement campaign described here. This field protocol is tailored to reduce the higher uncertainty ranges previously associated to melting calorimetry (Kawashima et al., 1998; Kinar and Pomeroy, 2015; Avanzi et al., 2016). It proposes a revised formulation of the calorimetric uncertainty that incorporates the calorimetric constant and the propagation of uncertainties coming from instrument, operational and environmental conditions. The uncertainty range associated with the new protocol for melting calorimetry is ±0.5% and the absolute error compared with Denothmeter measurements is ∼1% in volume.

2.1.5 Surface Roughness

Snow surface roughness controls the scattering behavior of the snowpack surface, with smooth surfaces exhibiting a dominant specular reflection and rough surfaces behaving more similarly to a diffuse scatterer. Snow surface roughness is typically expressed using three parameters: the root mean square of the heights (RMSH), the correlation lenght (CL) and the autocorrelation function (Williams and Gallagher, 1987; Nagler and Rott, 2000; Manninen et al., 2012; Anttila et al., 2014). These parameters can be obtained from a digitized snow transect. A proven and robust system involves inserting a panel into the snow and capturing images of the snow surface with a digital camera (Manninen et al., 2012; Anttila et al., 2014). For this campaign, we used the method described in Barella et al. (2021) and refined in Barella et al. (2025), which builds upon these concepts and it is particularly ~~apt~~ suited for field applications. The panel we used is made of black Forex, 70.5 cm wide and 47 cm tall. These dimensions are a trade-off between the ease of transport and the length of the snow transect covering at least 10 times the C-band wavelength λ=5.5 cm as suggested in (Manninen et al., 2012). The panel can be photographed by means of any digital camera. To attain a representative snow transect, 9 pictures were taken on each ~~campaign~~ measurement day: 3 along one direction, 3 along the perpendicular direction, and 3 at a 45° angle between them. The resulting roughness profile is averaged among all usable pictures, i.e., those not affected by excessive shadowing or unclean panel surface. To our knowledge, a time series of snow surface roughness properties was never measured before.

2.1.6 Snow Water Equivalent

Profiles of snow water equivalent (SWE) were sampled from the surface to the bottom with a cylinder cutter of inner diameter 9.44 cm and length 55 cm. The snowpack was sampled in sections from the surface to the ground and the total SWE was obtained by weighting each sample and summing up all the values. The uncertainty range of this instrument is around 10% with the main uncertainty source being caused by the presence of ice layers (Proksch et al., 2016).

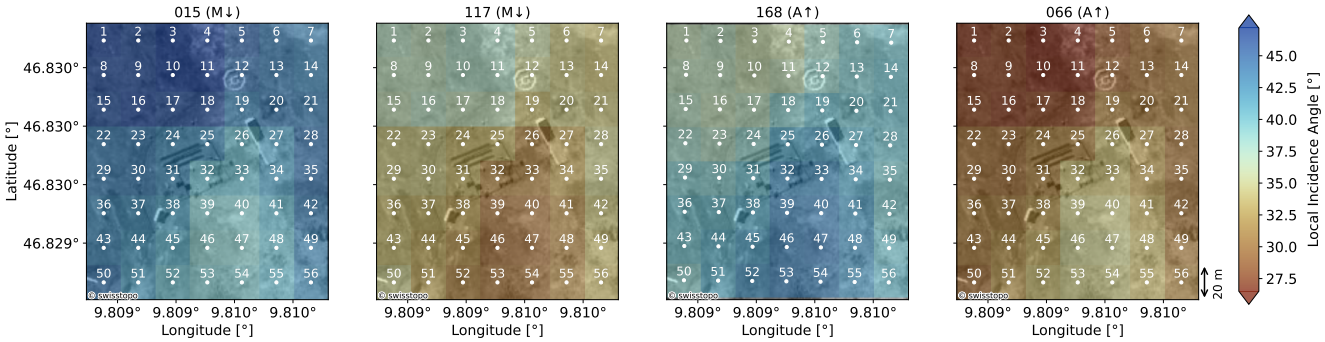

Figure 2. Overall range of local incidence angles across the study area for all the four relative orbits – morning/descending (M↓) and afternoon/ascending (A↑). Each S1 cell is identified by its centroid and a number.

2.2 Automatic measurements

2.2.1 Runoff

Runoff was automatically measured at a sub-hourly resolution by a lysimeter. Unfortunately, the instrument was discovered to be clogged when the runoff started in 2023. The instrument was repaired only in late May 2023. Therefore, the time series for that year starts with a peak (see Fig. 8d), although we hypothesize that runoff may have started as early as the end of April 2023. To avoid similar issues, on the following season the lysimeter was inspected timely and assessed as fully functional.

2.2.2 Snow Water Equivalent

Manual snow water equivalent (SWE) measurements are complemented by an automatically recorded time series at sub-hourly intervals, using the SSG1000 snow scale permanently installed at the WFJ site and manufactured by Sommer Messtechnik, Austria. The system consists of a weighing platform and load cells, which directly measure the weight of the snowpack on the platform and convert it into SWE. This instrument has a measurement range of 0 to 1000 mm of water equivalent. During the 2023-2024 snow season, the upper capacity was reached due to above-average snow depths. In comparison to manual measurements, Smith et al. (2017) estimated an error of $\pm 10\%$.

2.3 Sentinel-1 acquisitions

S1 is designed as a two sun-synchronous polar-orbiting satellite constellation, acquiring dual polarimetric C-band (frequency of 5.405 GHz, wavelength of 5.5 cm) SAR images with a nominal resolution up to 3.5 m × 22 m in Interferometric Wide swath mode (IW) and a revisit time of 6 days. Acquisitions in IW have a swat of approximately 250 km. This, together with the overlapping orbit paths, conceives the acquisition of multiple tracks at middle latitudes such as the Alps. For this reason,

within the time window of 6 days, more acquisitions of the same area may be available. ~~Four tracks are available for the area of Weissfluhjoch, and their main characteristics are summarized in Tab. 1.~~

~~List of Sentinel-1 tracks over the WFJ field site, with times of acquisition and incidence angles. Track number Time of acquisition Local incidence angle 015 Afternoon, ∼17:30 43° 066 Morning, ∼05: 30 31° 117 Afternoon, ∼17:30 33° 168 Morning,~~ Unfortunately, Sentinel-1B failed at the end of 2021, and with only Sentinel-1A in orbit, repeat cycles halved from 6 to 12 days. Since then, the overall data acquisition capability was reduced by ~~∼05:30 41°~~ 50% in most regions, including our Weissfluhjoch field site. Data from four relative orbits are available for this site: two ascending (afternoon) and two descending (morning) passes. Figure 2 shows the overall range of local incidence angles across the field site, which vary from a minimum of 27° to a maximum of 47°. These maps highlight domains with stronger and weaker dependence on the incidence angle – an east-facing back-slope and a flat area, respectively.

The SAR images can be downloaded, free of charge, from the copernicus data hub (Copernicus). To account for the complex topography and to reduce the speckle noise of SAR acquisitions, a tailored preprocessing procedure ~~has been~~ was applied to all data. The ~~procedure uses~~ processing procedure involves a combination of tools, some of which are available in SNAP (Sentinel Application Platform) version 6.0~~and some~~ , while others are customized and ~~written~~ developed in Python. The ~~procedure is listed and~~ full workflow is described in Marin et al. (2020); however, in this study, the gamma-MAP filter was not applied. The final spatial resolution of the post-processed S1 images is 20 × 20 m.

The nominal radiometric uncertainty of S1 falls in the range of 3σ=1.0 dB, as indicated in several ESA validation campaigns (Torres et al., 2012; Miranda et al., 2015; Schwerdt et al., 2017; Benninga et al., 2020). However, the overall radiometric accuracy is also affected by a number of preprocessing steps, including (but not limited to) the application of despeckle filters, terrain correction and radiometric normalization (particularly challenging in mountain regions with complex topography), and thermal noise removal (important in conditions of high absorption, such as wet snow). In such conditions, a detailed specification becomes extremely complex and falls beyond the scopes of this paper. Nonetheless, since this study explores the multitemporal behavior of σ_0^{VV} over a target cell, it is relevant to mention speckle denoising. We used the filter proposed by Quegan and Yu (2001) – a powerful yet relatively simple one to denoise multitemporal stacks, with a 11 × 11 pixels window. Similarly to local spatial multi-looking, its implementation involves local averages of intensity values for each date. Intuitively, this could potentially blur strong targets and edges, ultimately leading to a loss of resolution and impacting the overall multitemporal result. However, in conditions of dry snow, the snow cover and the position of the scatterers are stable, snow temperatures are well below 0°C and the soil should be mostly frozen, implying constrained variations in soil moisture. Under these conditions, the pixels we considered in our study exhibited an overall stable behavior. The same stability was observed during dry periods in summer. In these two cases, the standard deviation was within 1.0 dB, which aligns with the nominal radiometric uncertainty of S1. During the melting period, the primary source of radiometric uncertainty originates from the formation of LWC within the snowpack. As a consequence, the radar return signal from the same target cell changes over time, resulting in reduced temporal coherence and larger deviations in multitemporal statistics. As will be shown in the course of this study, LWC potentially exhibits high heterogeneity across a single resolution cell. Under such conditions, the estimation of radiometric uncertainty

becomes particularly challenging. Without a precise reference for LWC, a rigorous uncertainty quantification is inherently difficult and lies beyond the scope of this work.

2.4 Campaign design

Measurements were carried out within ~~the same snow pit, which was always dug anew starting at approximately~~ freshly dug snow pits, starting at 08:~~00.~~ 00 approximately. The start of the measurement procedure depended on the amount of employees available on a specific day, on the amount of snow, on its density and on the weather conditions – generally, between one to two hours later. The measurement procedure was generally finished around 12:00 refilling the snowpit; however, on isolated days, there were several hours of delay because of the above mentioned reasons. On the first snow season, the snow temperature was generally measured first and the melting calorimetry last, with the remaining measurements being carried out in between with an order that also varied as a function of the above mentioned factors. On the second snow season, we improved the campaign design with a more rigorous measurement order: temperature first, SSA and dielectric LWC either simultaneously or one after the other, density, SWE, and melting calorimetry coupled with a second simultaneous dielectric LWC profile taken at the same ~~time and~~ vertical location. This has specific importance for the LWC profiles. On the first season, the time lag between the dielectric and calorimetric LWC profiles was 2 or 3 hours, at an horizontal distance of 50 cm to 1 m. On the second season, we measured one first dielectric LWC profile and an adjacent, simultaneous one using melting calorimetry. In Sec. 4.2, we will refer to the first setup as "co-located" and to the second one as "simultaneous".

On both seasons, before starting the measurement procedure, the profile wall was made as smooth as possible. A Near-Infra-Red picture was taken for qualitative comparison. Outside of the snow pit, on an undisturbed area, the surface roughness panel pictures were taken. On days where the radiation (from the sun or diffuse) was particularly intense, shading was necessary for every surface measurement that might have been affected. The temperature profiles were always measured in the shaded corner area of the snow pit. Overall, each measurement series would need a total horizontal space of 1.5-1.8 m, and the single variable profiles were measured at a reasonable horizontal distance from each other. On both seasons, snow profiles were carried out within the same designated area. The area was divided in corridors approximately 2 m wide. Throughout the season, measurements were carried out moving continuously forward along the corridor until the slope was hit. The next snow profile would be dug onto the next corridor. A minimum distance of 30 cm was secured between two consecutive measurement days, to avoid disturbances from the previous measurement set.

Data cleaning and homogenization procedures were performed before providing the measured snow properties as RT inputs. In particular, since sampling resolutions were different (see Sec. 2.1), all measured properties were linearly interpolated to a common vertical resolution of 1 cm. Positive LWC values recorded at temperatures below 0°C were corrected to 0%. 0.04% and 0.4% of the measured LWC values were above or equal to 15% for the two years respectively. For both ~~used~~ dielectric instruments, these values are likely not accurate. Since these values likely represent areas of high snow wetness, they were not excluded from the analysis but their LWC value was set to 15%, similarly to Techel and Pielmeier (2011). Additionally, instances of very low LWC measurements from thin layers just above the ground in dry snow conditions were discarded, as we could not rule out potential instrument disturbances from the ground in these cases. Given the accuracy range of the

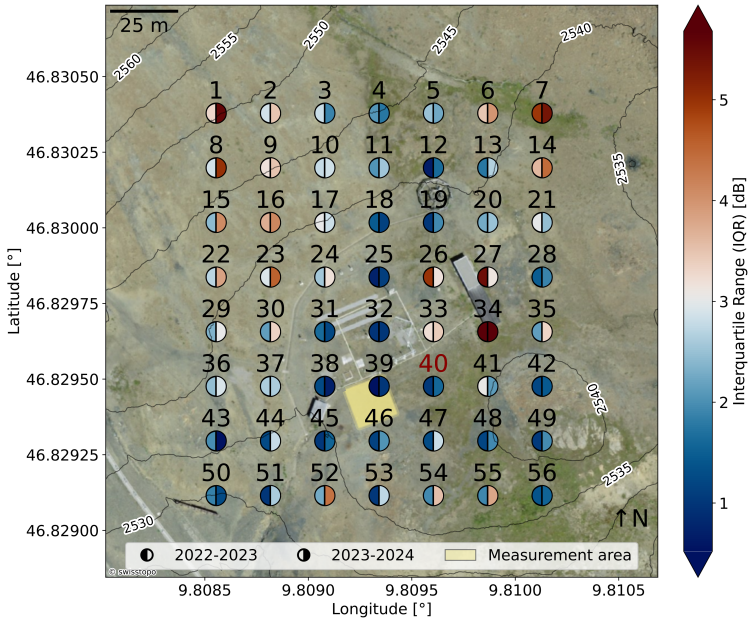

Figure 3. ~~The map in a) shows an aerial~~ Aerial view of the WFJ measurement station. Each of the 56 points represents the centroid of each S1 cell. Each centroid is split in two, the left part indicating the interquartile range (IQR) of the winter σ_0^{VV} signal for the snow season of 2022-2023 and the right part for the snow season of 2023-2024. Contour lines indicate the surrounding slopes. The ~~area in white indicates the surrounding skiable domain. The~~ yellow rectangle indicates the fenced measurement area where snow profiles were carried out in both seasons. Cell ~~39~~40, i.e. the selected S1 cell for this study, is highlighted in red.~~The boxplots in b) and c) represent the variability of σ_0^{VV} (in dry conditions) over different tracks for the fraction of the S1 cells having the 15% lowest IQR, for the snow seasons of 2022-2023 and 2023-2024, respectively.~~

thermometer (see Sec. 2.1), temperature oscillations up to 0.2~~°~~°C below 0~~°~~°C were set to 0~~°~~°C from the first measured fully isothermal profile onwards. Since the snow properties were measured at a certain lateral distance one from the other, the profiles of density and SSA were slightly shifted with a simple algorithm to maximise the correlation with the profile of LWC. Finally, we had to discard the last 3 ~~snowpits~~ snowpit measurements of 2023, because the measured RMSH value there was too high to ensure the conditions of validity of the interface model (see Sec. 3.2).

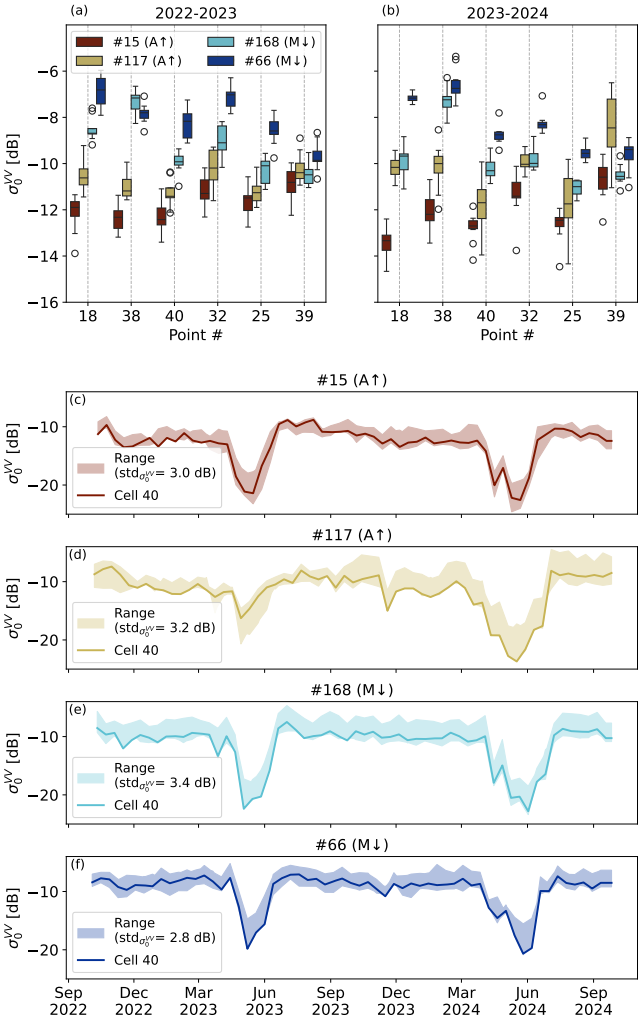

Figure 4. Variability of σ_0^{VV} in dry snow conditions for all relative orbits overlooking cells 18, 25, 32, 38, 39, 40, i.e. the flat terrain cells with likely similar snow properties as the measured ones (a-b). Multitemporal σ_0^{VV} signal of the selected cell 40 compared to the ensemble standard deviation ($std_{\sigma_0^{VV}}$) of the similar cells – morning/descending (M↓) and afternoon/ascending (A↑) (c-f).

3 Methods and model

3.1 Selection of the Sentinel-1 reference cell

The selection of the reference S1 cell required some considerations. The WFJ field site is ideal for continuous measurements due to its proximity to structures and sensors, however, these features may interfere with radar waves, thus disrupting the

Table 1. S1 tracks overlooking the selected cell 40, with times of acquisition, direction of orbit and local incidence angles.

Track #	Time of acquisition	Direction of orbit	Local incidence angle
015	~17:30	Ascending	41°
117	~17:30	Ascending	32°
066	~05:30	Descending	33°
168	~05:30	Descending	42°

~~backscattering~~ backscatter from natural terrain. Most of the structures within the field site are metallic and may act as additional reflecting sources in addition to the snowpack.

To select the reference cell, we extracted σ_0^{VV} values for both years over a grid of 56 points covering the whole extension of the field site and the immediate surroundings (Fig. 3~~a~~). For each cell and for each different year, we isolated the time frame starting at the beginning of the meteorological winter (~~December~~ Dec 01) and ending when the first liquid water was ~~detected~~ measured in the snowpack. Over these time frames, for each year and for each cell we computed the variability of σ_0^{VV} acquired by the 4 different tracks (See Tab. 1). We assume that ~~low variability~~ lower variabilities between different tracks over a dry snowpack may indicate a minimal interference with other non-natural elements on the field, as their backscatter would typically exhibit strong angular dependence (i.e., anisotropy).

The results of this analysis are ~~summarized~~ shown in Fig. 3~~. The~~ , where the variability is mapped over the field using the interquartile range (IQR). ~~Each cell is represented by its centroid. The boxplots in Fig. 3 refer to the fraction having the 15% lowest average IQR and illustrate the variability of σ_0^{VV} for each single track and over the two snow seasons independently.~~ In general, the IQR does not vary significantly between the two snow seasons, suggesting that this kind of approach might be adequate to select a reference cell with the least possible artificial disturbance. ~~There are outliers (~~Outliers – i.e.~~points~~ , cells 15, 22, 23, 27, 52, 54, and 55 ~~) – however, such points are located in field areas likely affected by double-bounces effects typical of~~ are likely influenced by localized field conditions. These include double-bounce effects typically associated with man-made ~~targets (~~structures (e.g., cell 27)~~or~~ , surfacing boulders (cells 52, 54, 55), ~~explaining the~~ or small variations in soil moisture, which could account for the observed year-to-year variability. The highest IQR values are clustered around the large hut (for double-bounce effects) and where the slopes start to become steeper ~~, i.e. where the backscattering has a strong~~ (when the backscatter has strongest dependence on the ~~aspect angle~~incidence angle). Interestingly, the IQR values for cell 25 and 32 are among the lowest for both snow seasons, suggesting that smaller metallic sensors might not represent a ~~disturbance for the~~ significant disturbance for radar waves. ~~The boxplots in Fig. 3 show the variability of each single track for both years, ordered from higher to lower. Cells 38 and 45, despite having low IQR score for both snow seasons, show high σ_0^{VV} variability among different tracks, suggesting that the small hut, being relatively small with respect to the resolution cell, likely has a limited impact with respect to the bigger hut, but still generates a bias. Ideally~~

Ideally, the target cell should coincide with the location of in-situ measurements to ensure that the observed snow properties accurately represent those detected by the radar. Although S1 footprint is large relatively to the area disturbed by a single snow

pit, excavating multiple consecutive snow profiles across a broader area can ultimately alter snow conditions across the entire cell – particularly under moist or wet snow conditions. This would introduce an uncontrolled degree of uncertainty. Therefore, the target cell ~~has a rather constant average σ_0^{VV} among all tracks and a~~ should rather be selected among the surrounding undisturbed cells with similar slopes and aspect. Fig. 4a-b show the dry-snow σ_0^{VV} variability for a set of cells with such features, i.e., cells 18, 25, 38, 39, 40. Among these, cell 40 shows a distinguished dependence on each incidence angle and orbit direction, along with relatively low variability of ~~each single track. These conditions are met by points 32,~~ σ_0^{VV} across tracks. An exception occurs for track #117 during 2023-2024, where the variability is relatively higher with respect to the year before. This increased variability is also noticeable for cell 25 and 39. ~~Points 25 and 32 were discarded because they lie on a section of~~ Given the lower variabilities recorded on the prior year, interference from non-natural elements can be ruled out. The most plausible explanation is a certain degree of heterogeneity in soil moisture across the field. Unfortunately, we are unable to verify this hypothesis, as soil moisture measurements were not included in our field campaign. Additionally, cell 40 lies in the ~~field where the snow surface is regularly disturbed for daily measurements until complete snow ablation. Point 39, despite slightly overlapping with our measurement area, lies in close proximity of the measuring field, on a flat surface, protected from off-piste skiing and exhibits the lowest average IQR, the lowest spread in~~ immediate vicinity to the measurement site, and the ~~average~~ snow surface remains undisturbed due to the operation of a LiDAR laser scanner continuously monitoring the snow surface. Fig. 4c-f illustrates the multitemporal σ_0^{VV} ~~value among all tracks, and the smallest overall variability of each single track, with a small exception for track~~ signal from cell 40 in comparison to that of the other candidate cells. The average standard deviation of the σ_0^{VV} ensemble across these cells is approximately 3 dB for all tracks. Interestingly, the lowest standard deviation is consistently observed at the time of the backscatter drop caused by wet snow, with the exception of track #117 ~~over the season 2023-2024~~in 2024. Notably, during the melting season, the signal from cell 40 lies in the lower end of the backscatter range across all years and tracks – aside for track #117 in 2022-2023. Potentially, this behavior is desirable for wet snow detectability. For these reasons, the σ_0^{VV} recorded over cell ~~39~~ 40 is selected as the reference time series for this work.

The impact of incidence angle was not a primary focus of this study, as it has already been extensively addressed in previous research Mätzler (1987); Shi and Dozier (1992); Strozzi et al. (1997); Strozzi and Matzler (1998), which strongly relied on tower-based instruments allowing greater control than satellite-based radar systems. In our case, the area most representative of measured snow properties is relatively small and flat, resulting in a limited range of local incidence angles available for analysis (see Fig. 2). Furthermore, the high spatial variability of LWC would require dedicated reference measurements for each incidence angle and cell, which was not feasible given the time and resources already involved in conducting the campaign at a single location.

3.2 Snow Microwave Radiative Transfer (SMRT) model: description and simulation setup

SMRT is a model that simulates the active-passive microwave response from ~~snowpacks (see Picard et al. (2018))~~layered snowpacks (Picard et al., 2018). The model is written and run in a Python environment and has a modular and flexible structure, allowing the user to set model runs choosing among ~~different~~ a wide set of electromagnetic, microstructure and permittivity models. The reflectivity and transmissivity associated to roughness can also be described according to different models.

The user has to specify a set of snowpack properties to parametrize the microstructure and the electromagnetic model. In particular, the roughness can be set either at the snow-air interface only or for each defined snow layer. Once these necessary parametrizations have been declared in the preliminary components of the model, SMRT uses the discrete ordinate and eigenvalue (DORT) method to solve the radiative transfer equation. The user can either customize a virtual sensor with specific frequency, incidence angle and polarization or directly choose from a list of already available sensors, among which ~~Sentinel-1. The backscattering~~ S1. The backscatter intensities can be obtained for all polarizations – this study focuses on the co-polarized ~~VV (vertical-vertical)~~ vertical signal, because cross-polarizations are currently only partially implemented within the current version of the module used for the parametrization of surface and interface scattering (Murfitt et al., 2024).

This study uses the symmetrized strong-contrast expansion (SymSCE) (Picard et al., 2022b) as the electromagnetic model with two different permittivity parametrizations. Measurements of density and SSA were used to compute the Porod length (ℓ_P) (Porod, 1951). The microwave grain size (ℓ_{MW}) is computed as the product of ℓ_P and the polydispersity k, a parameter describing the variability of the length scales with respect to the microstructure (Picard et al., 2022c). k was set to 0.75: this empirical value was estimated from μ-CT scans of a wide variety of ~~Alpine~~ alpine snow samples with convex grains, among which rounded grains and melt forms (Picard et al., 2022c). ~~As shown in Picard et al. (2022c), the choice of parametrization of the snow microstructure represents~~ For this study, snow microstructure was parametrized using the exponential model. For frequencies in the X- and Ku-bands (10-17 GHz), exponential auto-correlation functions have been shown to be too simplistic for representing snow microstructure. Their fast decay fails to capture long-range spatial correlations, and their inadequacy in modelling densely clustered media results in an underestimation of forward scattering effects (Chang et al., 2016). However, Picard et al. (2022c) show how ℓ_{MW} can be computed analytically for various forms of auto-correlation functions, including the exponential. These analytical expressions of ℓ_{MW} allow for direct comparison between different representations of snow microstructure. Most importantly, when the same value of ℓ_{MW} is used as input, all microstructure models give the same scattering amplitude in the low-frequency limit. Therefore, according to these findings, the choice of the best representation of snow microstructure becomes a secondary problem with respect to ~~the~~ measuring ℓ_{MW} in order to predict snow scattering ~~at~~ in the C-band~~. For this study, snow microstructure was parametrized using the exponential model~~.

The permittivity of a material is a complex number composed of a real part (i.e., the dielectric constant) and an imaginary part. The contribution of the real part is related to the material's ability to store electrical energy, whereas the contribution of the imaginary part is associated with dielectric losses. Snow is a three-component mixture of ~~snow~~ice, air and water – therefore, the effective permittivity of snow (ϵ_s) depends on the relative proportions of these elements. The presence of liquid water significantly alters both the real and imaginary parts of ϵ_s, affecting how microwaves interact with the snowpack. Henceforth, accurate estimates of ϵ_s are crucial for interpreting the microwave response of wet snow. Despite extensive research, particularly in the 1980s, a universally accepted model for snow permittivity ~~remains elusive~~ has not yet been established (Picard et al., 2022a). For this study, we selected two formulations: (i) the Microwave Emission Model for Layered Snowpacks ~~version~~ (Wiesmann and Mätzler, 1999) in its 3rd version (MEMLSv3 hereafter), which is based on the Maxwell-Garnett mixing theory of dry snow and prolate water inclusions; (ii) the Debye-like model modified by Hallikainen et al. (1986) ~~by fitting it against field data~~ (H-86 hereafter), which uses a mixing formula based on volume fractions and refractive indices, calibrated against

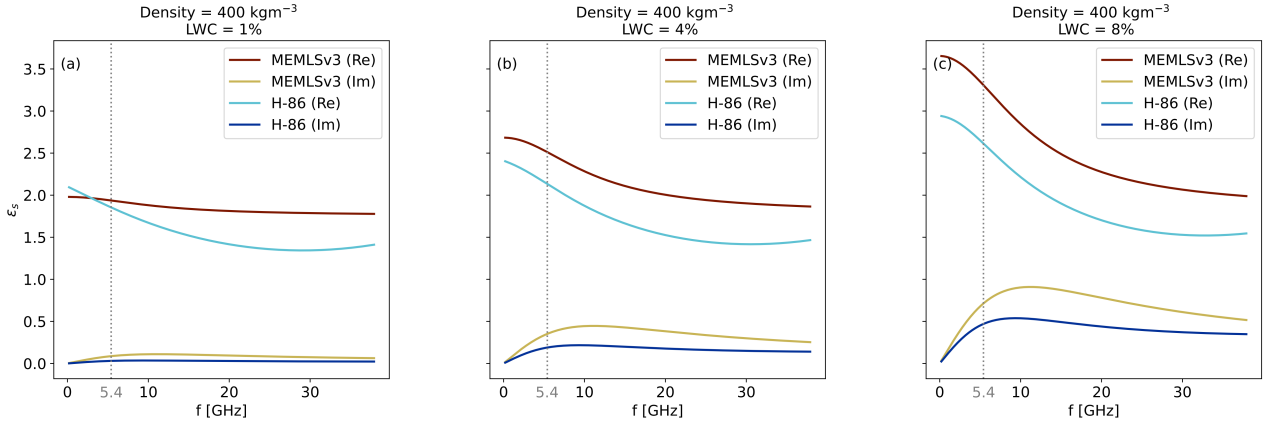

Figure 5. Real and imaginary parts of the effective permittivity (ϵ_s) of wet snow as a function of frequency (f) for a nominal density value of 400 ~~*kgm*$^{-3}$~~ kgm^{-3} and varying LWC of 1% (a), 4% (b) and 8% (c) according to the MEMLSv3 and H-86 permittivity models. Grey dotted lines underline differences between the formulations ~~for~~ at the nominal frequency of S1, i.e. 5.405 GHz.

field data. These models were selected because they ~~have been~~ were validated against real-world C-band data. Specifically, in Hallikainen et al. (1986) and earlier works, the authors present what is, to our knowledge, the only available dataset of wet snow permittivity measurements at 6 GHz for varying LWC values, measured using freezing calorimetry. Interestingly, ~~the~~ MEMLSv3 fails to accurately reproduce this dataset. However, Kendra et al. (1998) observed that the dielectric constant provided by H-86 appears to be too low, an observation that is supported by data from Achammer and Denoth (1994), collected in the range between 8 and 12 GHz. However, these data appear to favor H-86 over MEMLSv3 when considering the imaginary part of ϵ_s. While H-86 has been criticized, some aspects appear to have been overlooked (e.g. the recent corrigendum in Picard et al. (2022a)). Figure 5 shows the real and imaginary parts of the ϵ_s as a function of the frequency for a nominal density value and varying values of LWC according to both MEMLSv3 and H-86 permittivity formulations. For higher values of LWC (see Fig. 5b,c), the ϵ_s values obtained from both formulations display a frequency dependence and curve shape closely resembling that of pure water. In both cases, the real part of ϵ_s decreases with frequency, whereas the imaginary part increases up to the relaxation frequency and ~~then decreases~~ decreases thereafter. However, ~~at~~ in the C-band, the two formulations diverge significantly, especially in their prediction of the imaginary part, which governs absorption losses. This difference becomes more pronounced for increasing values of LWC. For instance, at ~~*LWC =*~~ LWC=4%, MEMLSv3 predicts an imaginary part of ϵ_s approximately twice that of the H-86 at the nominal frequency of S1 (see Fig. 5b). Since we cannot definitively determine the fitness of one model over the other, both formulations will be used in ~~the SMRT modeling~~ SMRT for this study. Given the different behavior of the two formulations, we expect a lower and upper bound for S1 ~~backscattering~~ backscatter simulations. It is clear that further research is needed to accurately characterize wet snow permittivity, but this is out of the scope of this paper.

RT modelling of snow comes with the additional difficulty of quantifying the dense medium effects, i.e., the electromagnetic interactions occurring between snow grains that are closely packed together. At C-band frequencies, these effects become significant as the scattering regime changes due to the presence of liquid water – both through changes in snow grain interactions and in bulk dielectric properties. In H-86, dense medium effects are not accounted for. In MEMLSv3, these effects are accounted through a semi-empirical parametrization involving, among other parameters, correlation length, density-dependent corrections and – as mentioned above – mixing formulas. Correlation lengths are used to represent the effective grain size and spatial correlation of the ice matrix, and to capture the degree of interaction between dense grains. Despite the range of correlation lengths being limited in MEMLSv3, the ones that are represented derive from structures observed at Weissfluhjoch during two snow seasons (Wiesmann and Mätzler, 1999). Therefore, they are likely suitable to describe the dense medium effects on the snowpack structures observed and measured in this study. Snow density is used as a proxy to determine how closely grains are packed; and as density increases, scattering is reduced and absorption increases. Such corrections are embedded into the extinction term, i.e., the sum of scattering and absorption coefficients.

The chosen interface model (between snow and air and between snow layers) is the integral equation model (IEM) (Brogioni et al., 2010), since it is one of the most used models to describe the roughness. However, any other model could be used, provided the roughness characteristics are within the validity range. The IEM is valid under the conditions $w \cdot RMSH < 2$ and $w^2 \cdot RMSH \cdot CL < \sqrt{\varepsilon_i}$, where w is the wavenumber (which depends on the medium) and ε_i is the ratio between the media permittivities at the interface (Fung et al., 1992). ~~In the absence of rigorous information about the soil substrate, we modeled it as a frozen surface . We parametrized the soil backscattering for each year and incidence angle with an average of the values recorded by~~

Using the functions available in SMRT, we modelled the substrate as a reflecting surface with a given value of backscatter. In dry snow conditions, on days when manual measurements and satellite overlooks coincided, we assigned the S1 ~~from the start of the meteorological winter until the formation of liquid water within the snowpack~~recorded backscatter value to the substrate, assuming that ~~in dry snow conditions, the snowpack is almost totally transparent to C-band radar waves ,~~ dry snow is transparent to radar waves at C-band and that therefore the soil is the only ~~scattering source~~contribution to the total backscatter. In wet snow conditions (or in dry snow conditions, when there was no concomitance between measurements and satellite overlooks), we assigned a fixed value of backscatter to the substrate, which we computed as the average value in dry snow conditions of each individual track (incidence angle). Notably, SMRT offers the possibility to compute the backscatter from the soil, however, it requires a series of detailed information that are spatially heterogeneous and would have been nearly impossible to retrieve continuously over the course of our campaign. These properties include the soil moisture, the relative sand content, the relative clay content, the soil content in dry matter, and other geometrical parameters such as the roughness and the correlation length.

Under these configurations, the model takes as inputs the following snowpack properties: temperature, density, volumetric liquid water, SSA and surface roughness. For the snow-air interface, we used the measured values of RMSH and correlation length. For layer interfaces, we set $RMSH_{layers}$=1 mm and CL_{layers}=30 mm (i.e., the average winter value from our field measurements). When measurements and S1 overpasses coincided, the simulation was performed using the incidence angle of

S1. On days without simultaneous overpasses, the simulation was performed using the incidence angle from the closest previous or subsequent S1 pass. All ~~modeling~~ modelling choices described above have been designed and motivated to be optimal to describe wet snow starting from measured properties. However, it is important to remark that the choice of such parametrizations remains highly arbitrary, as further research is still needed to validate permittivity, roughness and microstructure models specifically for wet snow ~~at~~ in the C-band.

Another practical challenge was ~~how~~ to design a way to replicate the often complex snowpack layering observed in the field within a radiative transfer model which is not specifically made to deal with a high number of layers thinner than the wavelength (Sandells et al., 2022). As a matter of fact, this increases the number of dielectrical discontinuities (Leduc-Leballeur et al., 2015) generating (artificially) higher scattering. Resampling high resolution field measurements to the wavelength or its multiples is an option, however, this does not necessarily reflect the physical snowpack structure. As an example, in the moistening phase, liquid water appears in thin layers ~~at the top~~ in the upper part of the snowpack. These layers can have thicknesses of a smaller size than the C-band wavelength ~~: their scattering effect~~ – the effect of such layers on the total backscatter is unclear and ~~this is~~ represents a potential source of errors when using layering defined by the resolution of the field measurements. As the wetting front progresses through the snowpack during the ripening phase, liquid water becomes more homogeneous over ~~thicker layers~~ layers with thickness comparable to the C-band wavelength. During this ~~phase, it might seem appropriate to choose~~ stage, using high-resolution discretizations (e.g., ~~comparable to~~ on the order of the C-band wavelength) ~~to reproduce as precisely as possible~~ may seem appropriate to closely replicate the liquid water layering observed in the field. However, ~~this may artificially produce drier or wetter layers, potentially leading to a over or underestimation in backscattering, respectively~~averaging over such scales can merge distinct wet and dry layers, blur important contrasts and potentially lead to biased backscatter estimates. On the other hand, intuitively, lower-resolution discretizations (e.g., multiples of the C-band wavelength) dissipate the scattering effect of thinner ($\simeq$6 cm) wet layers. To reduce the aforementioned sources of uncertainty, we chose to model the snowpack structure by stacking layers with a minimum thickness corresponding to the C-band wavelength, ensuring each layer had consistent average physical properties. These ~~property-based~~ physically similar layers were identified automatically by means of a simple algorithm and then refined manually, with particular emphasis placed on LWC over the other variables. An example is ~~given~~ provided in Fig. 6~~. However~~, where snow properties are shown at the field-measured vertical resolution in (a), and averaged into physically consistent layers for SMRT input in (b). Fig. 7 shows that the number of layers used for each SMRT simulation varied between 1 and 14, with a marked dependence on the stage of the melting process and on the campaign year. In dry snow conditions, the densely measured snow properties are practically always averaged into one single layer, given the absence of liquid water. As the snowpack starts moistening, the number of distinct layers increases, as a function of the first formation of liquid water within the snowpack. The highest number of layers required in SMRT to model the snowpack is used during the ripening phase, as the LWC layering is at its most heterogeneous state during this phase, as a consequence of the progression of the wetting front. Later in the runoff stage, with the snowpack being fully saturated, the number of used SMRT layers decreases again, as a consequence of a more homogeneously moist snowpack. On the other hand, Fig. 7 shows that during the ripening phase, the first campaign year has been modelled using $\sim$30% less layers than the second, on average. The presence of ice lenses helped to homogenize the distribution of liquid water within the snowpack, resulting in more uniformly wet

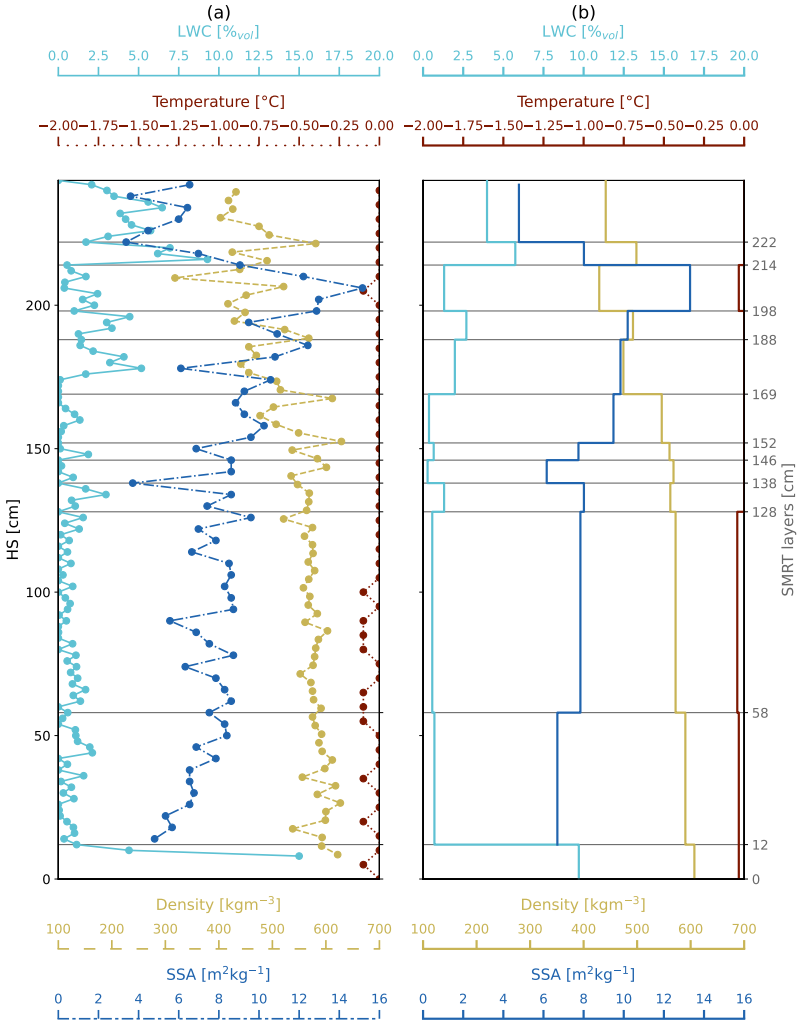

Figure 6. ~~Example of (a complete set)~~ Vertical profiles of ~~SMRT input snow~~ snowpack properties ~~for~~ measured in the field on May 14~~/05/~~, 2024: ~~measured~~ temperature (dark red), density (dark yellow), liquid water content (LWC; light blue), and ~~discretized with average values~~ specific surface area (~~brown~~SSA; dark blue)~~over identified physical~~ . The vertical spacing of the points connected by the lines reflects the measurement resolution for each profile: 5 cm for temperature, 3 cm for density, 2 cm for LWC, and 4 cm for SSA. (b) Representation of the same profiles averaged according to the physically consistent snow layers (~~yellow~~indicated by grey horizontal lines). The layered profiles as in (b) form the input snowpack for the SMRT model, combined with surface roughness parameters measured on the same day (RMSH=2.7 mm; CL=48.5 mm).

layers near the surface and consistently drier sections toward the bottom. Without ice lenses, in 2024, the progression of liquid water into the snowpack was more heterogeneous, therefore requiring more layers in the model to remain as true as possible to the conditions observed in the field. Despite the efforts to find a reasonable compromise between all the above mentioned

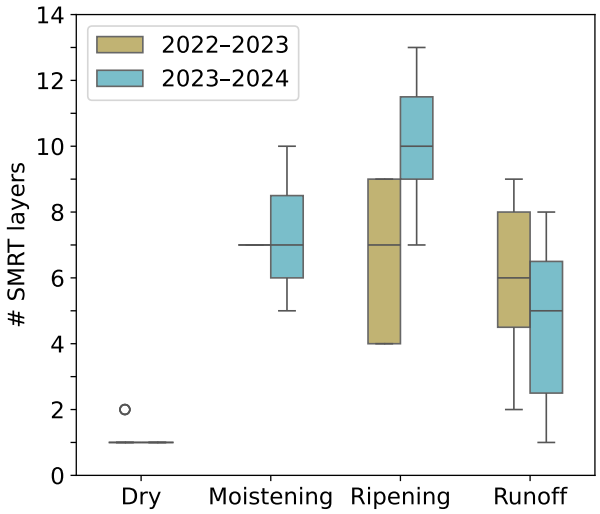

Figure 7. Variability of the number of modelling layers in SMRT used for each simulation day as a function of the melting phase and the campaign year.

constraints, the optimal way to model a radar-equivalent snowpack from field measurements and/or detailed multilayer physical model outputs remains an open question in the field of radiative transfer ~~modeling~~ modelling of snow, only recently addressed by Meloche et al. (2024), albeit for dry snow only.

4 Results

4.1 ~~Snowmelt~~ Identification and re-definition of melting phases ~~identification~~ from multitemporal Sentinel-1 ~~backscattering~~ backscatter and field measurements

Fig. 8~~and~~ -4.1 show the evolution of the multitemporal S1 SAR ~~backscattering~~ backscatter together with the time series of measured properties: snow temperature, LWC, air temperature, total water content (TWC), runoff, snow water equivalent (SWE) and surface roughness indices (RMSH and CL). The melting phases identified with the method proposed by Marin et al. (2020) are reported on each time series for later validation. We will refer to the snow seasons of 2022-2023 and 2023-2024 as the 2023 and 2024 seasons, respectively.

Our ~~measurement campaign brought us to observe that the roughness RMSH shows~~ roughness measurements show clear differences for different snow surfaces (Fig. 10). Smooth surfaces typical of new/dry snow have RMSH values around 1 mm (Fig. 10a). Thereon, ~~the RMSH~~ roughness increases with increasing surface degradation due to melt-refreeze cycles and sublimation (Fig. 10b). The values of RMSH measured in these conditions, which are the most persistent throughout the melt

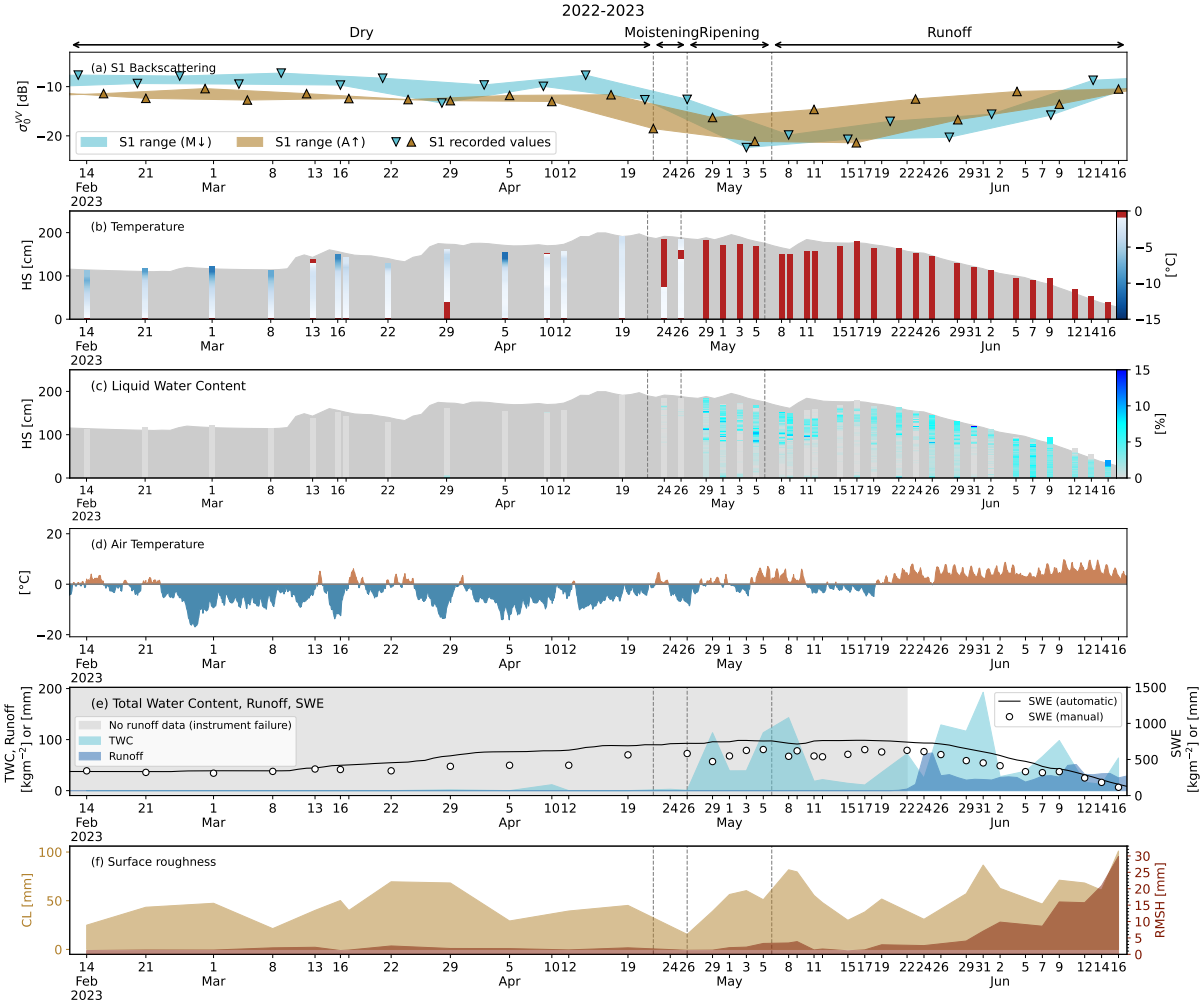

Figure 8. Data overview for the snow season of 2022-2023. ~~Panel~~ (a) ~~shows~~ S1 backscatter time series: exact values of σ_0^{VV} acquisitions (triangles); range obtained by connecting the ~~manually~~ consecutive S1 passages by direction of orbits, i.e. by connecting all the morning/descending (M↓) and the afternoon/ascending (A↑) acquisitions (shaded areas). Each panel is subdivided into the melting phases identified with the method of Marin et al. (2020). (b) Manually measured ~~temperature~~ profiles of snow temperature. ~~Panel~~ (~~b~~c) ~~shows the manually~~ Manually measured profiles of snow liquid water content (LWC)~~profiles~~. ~~Panel~~ (~~c~~d) ~~shows the air~~ Air temperature at hourly resolution~~as~~, measured by the automatic sensor at WFJ. ~~Panel~~ (~~d~~e) ~~shows the measured~~ Measured total water content (TWC) (light blue)~~, the~~ ; runoff time series automatically recorded by the lysimeter at WFJ (dark blue)~~,~~ ; lack of runoff data due to the instrument failure (grey area); snow water equivalent (SWE) both automatically recorded by the snow scale (black line) and manually measured (~~black points), and the lack of runoff data due to the instrument failure (grey area~~white circles). ~~Panel~~ (e) ~~shows the measured time~~ Time series of measured surface roughness ~~by means of the two indices~~ parameters – RMSH and CL.~~Panel~~

season, lie within 3 and 10 mm approximately. Fully-formed suncups are associated to values of RMSH around 10-15 mm (Fig. 10c). Deep suncups appear like craters on the snow surface (Fig. 10d), some reaching width of 20 cm and depths of 10 cm. In these conditions, we measured values of roughness RMSH equal or higher than 20 mm.

In 2023, the first liquid water was measured on Apr 10 ~~/04~~ (Fig. 8b~~,d~~). On this date, our data show that the temperature of the top ∼5 cm of the snowpack was 0~~°~~°C (Fig. 8~~a~~b). The air temperature reached 0~~°~~°C as well on this day (Fig. 8~~c~~d). The snowpack reached full isothermal state 20 days later. Ice layers formed throughout the season, likely as a consequence of repeated melt-refreeze cycles and the succession of several warm and cold spells (Fig. 8~~c~~d). Ice layers were observed regularly during the measurement campaign, their presence is highlighted by locally higher values of LWC due to ponding at approximately 100 cm from the ground. The presence of ice layers probably withheld the meltwater in the upper section of the snowpack, partially hindering the progression of the wetting front. LWC profiles in Fig. 8~~b~~ c highlight ponding above ice layers consistently until ~~15/05.~~ May 15. The ponding is no longer detected over the next consecutive 5 snow profiles and becomes visible again from May 26 ~~/05~~ until early June, when the ice layers likely disintegrated allowing the meltwater to percolate to the bottom of the snowpack. The fact that the ponding above ice layers is not detected on a series of consecutive snow profiles is probably linked to the partial refreeze of the snowpack highlighted by the drop in air temperature detected within this time span (Fig. 8~~c~~d). However, ice layers could also be laterally non homogeneous. Fig. 8f shows that the roughness associated with wet snow starts developing short after the snowpack starts moistening, with RMSH increasing until ~~09/05. Then, starting from 09/05~~May 9. Thereon, the cold spell brought new snowfalls which smoothened the snow surface significantly, and roughness indices reverted to typically winter values for approximately 10 days. Fully-formed suncups were observed on the field from May 31 ~~/05~~ onwards. As explained in Sec. 2.2, the lysimeter time series for 2023 (Fig. 8~~d~~e) is not useful to detect the runoff start. However, the automatic measurements indicate the first slight SWE decrease around ~~08/05~~May 8, following a warm spell that lasted several days. This occurred in the presence of a fully isothermal snowpack, suggesting that meltwater may have started to be released around this time.

In 2024, the first liquid water on the surface was measured on ~~08/04~~ Apr 8 during a warm spell (Fig. 4.1~~b,c,d~~b-d). From this date on, the wetting front moved somewhat into the snow before being interrupted by a cold spell, which caused a partial surface refreeze~~(Fig. 4.1a,b,c)~~. The snowpack reached the full isothermal state on ~~09/05.~~ May 9. Over the course of this season, ice layers were not observed in the field, the progression of the wetting front was not hindered and the snowpack reached full saturation earlier with respect to the previous year. The runoff time series confirms that the snowpack released the first meltwater around ~~08/04~~ Apr 8 – on this date, the (point-wise) measurements show a largely isothermal snowpack. Likely, the snowpack was isothermal over the entire cell (~~see~~ Fig. 4.1~~a,b,d~~b,c,e). Additionally, significant amounts of LWC were measured at the ground interface after ~~08/04~~ Apr 8 and the manual measurements show a SWE decrease of ≃100 mm between ~~04 and 15/04.~~ Apr 4 and 15. These observations can validate the same hypothesis made for the previous season in the absence of runoff data due to instrument failure. Our measurements in Fig. 4.1~~e shows that we measured increasing surface roughness~~ f show that surface roughness increased relatively late (~~03/06~~Jun 3) with respect to the previous season, with fully-formed suncups being visible on the field from Jun 19 ~~/06~~ onwards.

Coupling the detailed, high temporal resolution information about the state of the snowpack with the multitemporal SAR σ_0^{VV} recorded by S1 on morning and afternoon overpasses (Fig. 8-4.1~~f~~a) enables the validation of the methodology proposed by Marin et al. (2020) to identify the melting phases. According to the authors, a drop of at least 2 dB with respect to the winter mean in the afternoon/ascending σ_0^{VV} identifies the start of the moistening phase; the ripening phase starts when the morning/descending σ_0^{VV} signal shows the same drop of at least 2 dB; the runoff starts when both morning~~and afternoon /descending~~ and afternoon/ascending σ_0^{VV} time series reach their local minima before the monotonic increase (the authors propose an average date between the two local minima when both the S1 satellites were available). ~~To obtain~~ For the two seasons, we computed the average winter ~~backscattering~~ backscatter ($\overline{\sigma_{0,dry}^{VV}}$) ~~for the two seasons, we considered~~ by averaging all values recorded by ~~all tracks over the~~ each individual track over the course of the meteorological winter, i.e.~~from~~ , from Dec 01 ~~/12 until 28/02. This is the threshold~~ to Feb 28. The resulting values are the benchmark needed to identify the melting phases~~, which are summarized in Table~~ . The results are listed in Tab. 2. As noted by Marin et al. (2020), the dependence of σ_0^{VV} on incident ~~and aspect~~ angles remains as a residual effect. ~~While the overall magnitude does not change significantly, it would be more precise, in theory, to compute four separate values for $\sigma_{0,dry}^{VV}$, one for each track. However, our selection of the reference cell was guided by minimizing the influence of aspect and incidence angles on the winter σ_0^{VV} as discussed above (see Fig.3b). As a result, we chose to use a single, averaged value of $\overline{\sigma_{0,dry}^{VV}}$ over the 4 tracks.~~

~~Overview on the identification of the melting phases based on the multitemporal S1 SAR backscattering as proposed by Marin et al. (2020). For each season, the table shows the relevant values of σ_0^{VV} and the occurrence dates. For the runoff start, the date proposed by Marin et al. (2020) is compared against the data from the lysimeter, when available.~~

Because for the selected cell two morning/~~04 -12.5 04~~descending and afternoon/~~04 Ripening start -13.2~~ ascending looks are available, there are two possible dates for the start of the moistening and ripening phase, respectively. In 2023, these dates are Apr 22 and 29 for the moistening phase and Mar 28 and Apr 26 ~~/04 -16.9 15/04 $\sigma_{0,min,afternoon}^{VV}$ -18.7 16/05 -20.6 10/05 $\sigma_{0,min,morning}^{VV}$ -19.9 03/05 -19.9~~ for the ripening phase. For the start of the moistening phase, we selected the earliest, i.e. Apr 22. For the start of the ripening phase, the two identified dates are almost one month apart, however, the σ_0^{VV} decrease recorded on Mar 28 by track #168 derives from a melt-refreeze cycle, as the following value recorded by the same track aligns back around the winter mean. Therefore, we selected Apr 26 ~~/05 Marin et al. (2020) Lysimeter Marin et al. (2020) Lysimeter Runoff start 09/05 No data – ~29/04 (?) 18/05 ~15/04~~

~~The method of Marin et al. (2020) is challenged by the low S1 revisit frequency provided by only one satellite. In detail~~as the start of the ripening phase. In 2024, for the moistening ~~start in 2023,~~ phase, the σ_0^{VV} ~~recorded on 17/~~value recorded on Apr 04 by track #015 is only 1.5 dB lower than $\overline{\sigma_{0,dry}^{VV}}$, ~~whereas on~~ however, the next passage ~~the drop is 7.8 dB already . For this reason~~of the same track on Apr 16 recorded a drop of already 7.4 dB. Therefore, the moistening start ~~for 2023~~ has been placed on ~~the date in between, namely 19/~~Apr 04. ~~Moreover, due to the lower satellite revisit time, the separations~~ On this date, track #117 recorded a drop of 7 dB with respect to $\overline{\sigma_{0,dry}^{VV}}$. For the ripening start, we chose Apr 15.

These considerations show that the method of Marin et al. (2020) is limited by the the halved S1 revisit frequency. This becomes even more clear for the selection of the runoff start date, as the wider separation between local minima ~~are 13 and 16~~ of σ_0^{VV} considering all 4 looks is 17 days for 2023 and ~~2024, respectively.~~ 16 days for 2024. Using the date in between

Table 2. Overview on the identification of the melting phases based on the multitemporal S1 SAR backscatter as proposed by Marin et al. (2020). For each season, the table shows the relevant values of σ_0^{VV} and the occurrence dates for each afternoon/ascending (A↑) and morning/descending (M↓) look (and corresponding incidence angle). The selected values for the start of the moistening, ripening and runoff phases are highlighted in bold. For the runoff start, the selected date according to the method of Marin et al. (2020) is compared against the data recorded by the lysimeter, when available.

~~Season → Event ↓ dBDate dBDate $\overline{\sigma_{0,dry}^{VV}}$ -9.7 01/12 - 19/04 -10.4 01/12 - 04/04 Moistening start -11.2 ~ -17.5~~

Season	**2022-2023**				**2023-2024**			
Track	015 (A↑)	117 (A↑)	066 (M↓)	168 (M↓)	015 (A↑)	117 (A↑)	066 (M↓)	168 (M↓)
Local Incidence Angle	41°	32°	33°	42°	41°	32°	33°	42°
$\overline{\sigma_{0,dry}^{VV}}$ *[dB]*	-12.3	-11.4	-8.4	-10.0	-12.6	-11.5	-8.9	-10.1
Moistening start date	**Apr 22**	Apr 29	–	–	**Apr 04** – Apr 16	Mar 18	–	–
Moistening start value [dB]	-18.5	-16.3	–	–	-14.1 – -20.0	-13.9	–	–
Ripening start date	–	–	**Apr 26**	Mar 28	–	–	Apr 08	**Apr 15**
Ripening start value [dB]	–	–	-12.6	-13.3	–	–	-12.8	-17.9
$\sigma_{0,min}^{VV}$*, date*	May 16	Apr 29	May 08	May 03	May 22	May 17	May 26	Jun 02
$\sigma_{0,min}^{VV}$*, value [dB]*	-21.4	-16.3	-19.8	-22.4	-22.6	-23.7	-20.7	-22.8
Runoff start date (Marin et al., 2020)	**May 06**				**May 24**			
Runoff start date (Lysimeter)	No data – ∼Apr 29 (?)				∼Apr 15			

to determine the runoff start, as done by Marin et al. (2020), gives potentially unreliable results in these conditions. This low temporal resolution makes it difficult to pinpoint precise onset dates, especially when minima are separated by such long periods. Despite the ambiguities, on both seasons, the identified moistening phase coincides exactly with the first snowpack warming and the consequent formation of liquid water. The identified ripening phase is also mostly consistent with the theory, as field measurements show that the snowpack transitions to the fully isothermal state with the wetting front progressing to the bottom, although this process is partially hindered in 2023 by ice layers. In 2024, a sudden cold spell at the beginning of the ripening phase caused the refreezing of the superficial meltwater (Fig. 4.1~~a,b,c~~b-d). This generated a sharp increase in both morning and afternoon σ_0^{VV} (Fig. 4.1~~f~~a). In 2024, the first instance of measuring a fully isothermal snowpack coincided precisely with the first afternoon local minimum of σ_0^{VV}. The ~~positive bias of the track 117 due to its low incidence angle does not allow to verify the same~~ same cannot be verified for 2023~~and it creates~~ , which instead shows a counterintuitive case where the local minimum of morning σ_0^{VV} anticipates the local minimum of afternoon σ_0^{VV} (Fig. 8~~f~~a). Nonetheless, by the time the morning σ_0^{VV} reached its local minimum in 2023, the snowpack had already been fully isothermal for at least 5 days (Fig. 8~~a,f~~a-b). This suggests that the snowpack is likely to be fully isothermal when the afternoon ~~backscattering~~ σ_0^{VV} reaches its local minimum. The runoff time series in 2024 shows that the snowpack had started to release meltwater as soon as in the late moistening phase (Fig. 4.1~~d~~e), in correspondence of the first local minimum of the ~~multitemporal SAR backscattering on~~ afternoon σ_0^{VV} time series on Apr 16 ~~/04~~ (Fig. 4.1~~f~~a).

Marin et al. (2020) proposed three possible explanations for the monotonic ~~backscattering~~ backscatter increase following the local minima: (i) the increase in surface roughness, (ii) the decrease in TWC and (iii) the snow cover gradually becoming patchy. Our data show that over a high-altitude alpine snowpack like the study plot at WFJ, ~~surface roughness develops well in advance of when~~ roughness develops on the snow surface well before the snow cover begins to disappear in patches. Therefore, at least for similar altitudes, the gradual disappearance of the snow cover can be ruled out as a cause of the increasing ~~backscattering~~ backscatter in the late melting stage. For both seasons, our data indicate that the strongest correlation with the monotonic increase of σ_0^{VV} after the local minimum is observed with the gradual increase in surface roughness (Fig. 8-4.1~~e~~f). Conversely, there seems to be no remarkable correlations between the increase in σ_0^{VV} and the TWC and/or runoff trends. In fact, Fig. 8-4.1~~d~~ e show that the decrease of TWC as a consequence of snow ablation is not monotonous. On the other hand, both automatic and manual measurements show that by the time SWE started decreasing monotonically (around May 26~~/05/2024 and 06/~~, 2023 and Jun 06~~/~~, 2024), the S1 σ_0^{VV} had already increased again by $\simeq$~~5~~ 6 dB.

4.2 Instrumental uncertainty and variability in field measurements of liquid water content

Fig. 5 shows that liquid water has a strong impact on the real and imaginary parts of ~~the effective permittivity of snow~~ ϵ_s at C-band frequencies~~, and therefore, on radiative transfer modeling~~. For S1 σ_0^{VV} retrievals from ground measurements, this poses three major challenges. In the first place, manual measurements concern a very small area/volume whereas satellite acquisitions cover a pixel size of 20 × 20 m. Secondly, the distribution of liquid water within the snowpack can be highly heterogeneous because of a variety of features and processes, namely capillary barriers, preferential flows, ice layers. Finally, what is the most accurate methodology for measuring LWC in both lab and field environments remains a debated question in snow science (Barella et al., 2024), and although the methods used in this paper ~~attempt~~ were designed to achieve a good level of ~~reliability~~robustness, they are nevertheless subject to error. Therefore, all these uncertainty sources need to be taken into account when comparing satellite σ_0^{VV} ~~retrievals with~~ signatures with retrievals driven by measured data.

In Sec. 2.4, we explained how dielectric measurements were validated against melting calorimetry in conditions of ripe snow. We referred to the validation setup of 2023 as "co-located" only; whereas in 2024 we performed an additional "simultaneous" validation in addition to the co-located. Figure 11 shows the spread between dielectric and calorimetric measurements in co-located and simultaneous setups for all the LWC validation measurements made over the two years. In 2023, the average maximum bias between co-located measurements is 2.6% and the average standard deviation is 1.2%. In 2024, the average maximum bias and the average standard deviation are 2.6% and 1.4% for co-located measurements and 2.3% and 1.5% for simultaneous measurements, respectively. Figure ~~??~~ 13 shows all the measured vertical profiles in detail. In 2023, there is an overall good agreement between dielectric and calorimetric measurements. The time lag between the measurements is highlighted by often similar LWC profile shapes, with calorimetry generally measuring higher peak values. Unexpectedly, in 2024, the simultaneous measurements resulted in only slightly lower biases and slightly higher standard deviations. This counterintuitive result is supported by a number of previous studies. For example, Donahue et al. (2022) found an average standard deviation of 1% over 10 cm wide snow samples with LWC between 0 and 5%. The study of Techel and Pielmeier (2011) confirms the high occurrence of measurement deviations of more than 1% at short horizontal distances. However, Techel

and Pielmeier (2011) also show that the correlation between measurements at larger horizontal distances is higher for LWC values lower than 1.3%. Therefore, the biases and standard deviations observed in our field measurements may overestimate the instrument uncertainty and/or variability over larger scales comparable to the footprint of S1. Based on these considerations, we define the large-scale LWC variability as $\pm 1\%$. We use this value to assess the effect of LWC uncertainty on σ_0^{VV} retrievals from ground measurements.

4.3 Interpretation of Sentinel-1 ~~backscattering~~ backscatter through SMRT simulations ~~driven~~ forced by field measurements

~~Figure~~ Fig. 12 shows the comparison between the time series of S1 acquisitions and ~~the modeled~~ SMRT-modelled σ_0^{VV} ~~driven~~ forced by snowpit measurements using the two different permittivity ~~models~~ formulations (MEMLSv3 and H-86~~in SMRT~~) and the model setup described in Sec. 3.2, considering the LWC variability of $\pm 1\%$ estimated in Sec. 4.2. In this Figure, ~~we divided the simulation results into groups and discuss possible driving mechanisms~~ together with Tab. 3, simulation results are categorized into groups, and potential sources of inconsistencies and/or ~~deviations from S1~~ driving scattering mechanisms are discussed for each group, based on the measured values of LWC, TWC, and surface roughness. ~~We show all~~ All measured profiles of LWC~~with the relative measured values of~~ , along with the corresponding TWC and RMSH values, are presented in Fig. 13 and Tab. 5, which ~~will~~ serve as a reference ~~in the following explanations~~for the following analysis. Tab. 4 shows all ~~biases~~ the Root Mean Squared Errors (RMSE) between S1 acquisitions and simulations, according to the snow season, the selected permittivity formulation and the melting phase. In general, both models exhibit a mean negative bias of ~~6~~ ≃5 dB with respect to S1 recordings over both seasons; however, biases are more pronounced for 2024 than for 2023, with the deviation between permittivity models being higher as well in 2024. H-86 generally gives higher σ_0^{VV} values with respect to MEMLSv3.

In 2023, the #066 morning S1 track recorded a ~~backscattering~~ backscatter increase of more than 2 dB between Apr 05 and ~~19/04.~~ 19. Similarly, in 2024, we observe a 2.5 dB increase in ~~backscattering~~ backscatter recorded track #117 from Feb 08 ~~/02 to 04/03.~~ to Mar 04. We can hypothesize that such increases are driven by the thawing of the soil. However, our data are insufficient and too uncertain to prove so, because of ~~the~~ possible interferences between dielectric instruments and the ground in mostly dry snow conditions, as mentioned in Sec. 2.1.4. In dry snow conditions, there were no significant discrepancies between S1 and simulations~~during the dry seasons~~; henceforth Fig. 12 only focuses on the period after the assumed soil thawing.

Aside the chosen permittivity ~~model~~formulation, five primary sources of uncertainty may account for the differences between simulated and recorded σ_0^{VV}. ~~In the first place, we should consider the fact that a significant source of uncertainty between recorded and modeled σ_0^{VV} values~~ A significant one is snow transformation and melting between satellite and measurement acquisitions. S1 orbits intersect the field area either in the early morning or in the late afternoon (see Tab. 1). As explained in Sec. 2.4, measurements started at around 10:00 and would take several hours. Thus, it is likely that in both cases the LWC during the passage is lower than the value measured at 10:00 or later because of daily melt-refreeze cycles, especially near the snowpack surface. Moreover, the point-wise LWC measurements are not necessarily representative of the general liquid water distribution ~~on~~ over the entire S1 ~~pixel~~cell. In 2023, we consistently observed ice layers over a high number of consecutive

Table 3. ~~Bias~~ Supplementary information to Fig. 12: measured values of TWC, LWC, RMSH, noteworthy events for scattering (~~in dB~~such as cold spells or late snowfalls)~~between modeled~~ , and ~~S1 recorded σ_0^{VV} values according~~ explanations to the ~~snow season, the selected permittivity formulation~~ mismatch between modelled and ~~melting phase~~recorded S1 backscatter signatures.

Group	TWC	LWC	RMSH	Event	Source(s) of inconsistency, scattering mechanism
1a	–	–	–	Soil thawing	– Backscattering increase due to soil thawing
2a	<10 mm	<3%	1 mm	Snowpack moistening Smooth surface	– Uncertainty in spatiotemporal LWC/TWC – Scattering from surface structures (melt-refreeze) – Surface roughness underestimation – Wet soil scattering
3a	>10 mm	>3%	1→4 mm	Snowpack ripening Formation of surface roughness	– Uncertainty in spatiotemporal LWC/TWC – Uncertainty in surface roughness measurements – Uncertainty in IEM modelling
4a	>10 mm	>3%	3∼4 mm	Snowpack ripening Increasing surface roughness	– Uncertainty in spatiotemporal LWC/TWC – Uncertainty in surface roughness measurements – Uncertainty in IEM modelling
5a	>10 mm	>3%	∼1 mm	New snowfall on a wet snowpack Well-developed surface roughness	– "Buried surface roughness"
6a	<10 mm	<3%	∼1 mm	Cold spell (partial snowpack refreeze) Smooth surface	– Uncertainty in spatiotemporal LWC/TWC – Scattering from surface structures (melt-refreeze) – Uncertainty in surface roughness measurements – Wet soil scattering
7a	>10 mm	>3%	>4 mm	Wet snowpack Fully-formed suncups	– Uncertainty in spatiotemporal LWC/TWC – Uncertainty in surface roughness measurements – Uncertainty in IEM modelling
1b	<10 mm	<3%	∼1 mm	Snowpack moistening Smooth surface	– Uncertainty in spatiotemporal LWC/TWC – Scattering from surface structures (melt-refreeze) – Surface roughness underestimation – Wet soil scattering
2b	>10 mm	>3%	∼1 mm	Snowpack moistening Smooth surface	– Uncertainty in spatiotemporal LWC/TWC – Scattering from surface structures (melt-refreeze) – Surface roughness underestimation
3b	<10 mm (Varying)	<3%	∼1 mm	Cold spell (partial snowpack refreeze) Smooth surface	– Uncertainty in spatiotemporal LWC/TWC – Scattering from surface structures (melt-refreeze) – Surface roughness underestimation – Wet soil scattering
4b	>10 mm	>3%	∼1 mm	Snowpack ripening Smooth surface	– Uncertainty in spatiotemporal LWC/TWC – Scattering from surface structures (melt-refreeze) – Surface roughness underestimation
5b	>10 mm	>3%	∼3 mm	Snowpack ripening Increasing surface roughness	– Uncertainty in spatiotemporal LWC/TWC – Uncertainty in surface roughness measurements – Uncertainty in IEM modelling
6b	>10 mm	>3%	∼1 mm	New snowfall on a wet snowpack Well-developed surface roughness	– "Buried surface roughness"
7b	>10 mm	>3%	>4 mm	Wet snowpack Fully-formed suncups	– Uncertainty in spatiotemporal LWC/TWC – Uncertainty in surface roughness measurements – Uncertainty in IEM modelling

Table 4. RMSE (in dB) between modelled and recorded σ_0^{VV} values according to the snow season, the selected permittivity formulation and melting phase.

Season → Permittivity formulation → H-86 MEMLSv3 Data to compare H-86 *Season*	MEMLSv3	2022-2023	Data to compare
Bias ↓ height *Permittivity formulation*	dB**H-86 [dB]**	dB**MEMLSv3 [dB]**	#**Data to compare** [
Overall height *Overall*	5.37 3.4	6.57 4.5	12 9
Dry *Dry*	1.00 0.5	1.35 0.7	5
Moistening *Moistening*	–	–	0
Ripening *Ripening*	5.17 5.8	6.96 7.6	4 3
Runoff *Runoff*	8.84 0.2	10.24 1.9	3 1

snow profiles (see Fig. 8b c and 13). Our consecutive measurements suggest that ice layers contributed to creating a more spatially homogeneous liquid water distribution by acting as a natural drainage barrier for meltwater. Unlike 2023, in 2024 ice layers were not consistently observed in the field. Likely, the melting process has been was more heterogeneous over the cell area of 20 × 20 mS1 cell, and point-wise measurements are less representative of wider scales on in this season. This explains the fact that days marked by high variability associated with LWC are more numerous in 2024 than in 2023. In Fig. 12Tab. 3, we grouped these sources of uncertainties together under the labels "uncertainty in spatiotemporal LWC/TWC". Potentially, this source of uncertainty affects every S1 retrieval from field data. However, it definitely carries more weight than other sources of error at early melt stages when the simulation variability associated to LWC uncertainty is particularly high, i.e., when the TWC is low (24 to 26/04/2023, 04/Apr 24-26, 2023; Apr 04/, 2024) and during both the cold spells of 2023 (May 17/05) and 2024 (15 to 23/04Apr 15-23), which caused the partial refreeze of the snowpack (see Fig. 8-4.1a,b, c, 4.1b-d).

Daily melt-refreeze cycles, however, not only alter the amount of LWC/TWC in the snowpack, but they also drive the formation of surface structures that can create additional scattering which is not accounted for in the simulations, i.e. crusts (Lund et al., 2022; Brangers et al., 2024). In Fig. 12Tab. 3, we labeled this uncertainty source as "scattering from surface structures due to (melt-refreeze)". This uncertainty applies to the same cases as where "uncertainty in spatiotemporal LWC/TWC" applies, but it likely holds more weight when the TWC is slightly higher and the simulation variability according to LWC is lower (08 to 15/04/2024, Apr 08-15, 2024; Apr 27 /04 to 09/- May 05/, 2024).

Another cause of significant discrepancy between recorded and modeled modelled σ_0^{VV} in the presence of a mostly dry snowpack with a smooth surface may be the thawing of the soil. This process creates a thin layer of liquid water overlying the natural soil roughness or absorbed into the basal snow layer (Lombardo et al., 2025). The combination of snow wetness and roughness, as will be shown later in the paper, can be responsible for backscattering backscatter increases up to 7 dB. In Fig. 12 Tab. 3 we refer to this kind of uncertainty as "scattering from the wet soil wet soil scattering". This uncertainty potentially applies to the instances when the TWC is relatively low and the variability associated to LWC is high. Between 04 and 27/04/Apr 04-27, 2024, our measurements show considerable amounts of liquid water at the soil interface with otherwise relatively dry snowpack and smooth surfaces (see Fig. 13). The lysimeter time series corroborates these measurements by

Table 5. Total ~~Water Content~~ water content (TWC) and ~~Surface Roughness~~ surface roughness (RMSH) values measured ~~on the same dates as~~ for the LWC profiles shown in Fig. 13.

2023			2024		
Date	**TWC [mm]**	**RMSH [mm]**	**Date**	**TWC [mm]**	**RMSH [mm]**
Apr 24	3	3	*Apr 04*	2	1
Apr 26	1	1	*Apr 08*	13	2
Apr 29	113	1	*Apr 11*	14	1
May 01	39	2	*Apr 15*	34	2
May 03	39	2	*Apr 16*	6	–
May 05	114	3	*Apr 18*	3	1
May 08	143	3	*Apr 23*	4	2
May 09	102	4	*Apr 27*	11	1
May 11	18	1	*May 02*	16	2
May 12	22	2	*May 09*	161	1
May 15	14	1	*May 10*	62	2
May 17	11	1	*May 14*	46	3
May 19	36	3	*May 21*	96	1
May 22	72	–	*May 22*	110	1
May 24	24	3	*May 29*	80	2
May 26	129	–	*Jun 03*	145	4
May 29	116	4	*Jun 07*	115	3
May 31	193	7	*Jun 10*	44	4
Jun 02	27	10	*Jun 14*	47	6
Jun 05	38	–	*Jun 19*	129	14
Jun 07	67	9	*Jun 22*	71	12
Jun 09	98	16	*Jun 26*	63	–
Jun 12	16	16	*Jun 27*	42	12
Jun 14	13	21	*Jul 01*	22	14
Jun 16	64	30	*Jul 04*	29	13

detecting runoff start on Apr 08~~/04/~~, 2024 (see Fig. 4.1~~d~~e). However, we lack sufficient data in order to prove and explore this possible scattering source, therefore we ~~mention it only~~ only mention it as an hypothesis.

Two similar instances in 2023 (~~05 to 09/05~~May 05-09) and 2024 (Apr 10 and 14~~/05~~) suggest another interesting phenomenon likely affecting simulation accuracy. On both these intervals, Fig. 12 shows very good agreement between recorded and ~~modeled~~ modelled values of σ_0^{VV}, regardless of the chosen permittivity model and the variability associated to LWC. ~~On~~ In both instances, surface roughness had just started developing on a wet snow surface (~~*LWC* >~~LWC>3%), with measured RMSH values between 3 and 4 mm (see Fig. 10b). Thereafter, spring snowfalls cover the early-stage roughness and the snow surface reverts to smooth with RMSH values between 1 and 2 mm (see Fig. 10a). On both years, the group of simulations following the spring snowfalls (i.e. ~~11 to 15/05/~~May 11-15, 2023~~and ~~; May 21 and 22~~/05/~~, 2024) show again strong biases when compared to S1 recordings. This bias is almost certainly due to the fact that the surface roughness which had started to develop ~~is now~~ was then buried below a smooth layer of new snow and it is not simulated by SMRT in the proposed configuration (see Sec 3.2). In ~~Fig. 12~~ Tab. 3 we labeled this phenomenon as "buried surface roughness".

Generally, simulations are in better agreement with S1 recordings when the measured surface RMSH is above 3 mm. Fig. 12 shows multiple groups of simulations where S1 retrievals from field data gain increasing accuracy with increasing RMSH on a wet surface, together with a decreasing dependence on the chosen permittivity model and the uncertainty associated to LWC (Apr 29 ~~/04 to~~ to May 09~~/05/2023, ~~, 2023; May 19 ~~/05 to~~ to Jun 09~~/06/~~, 2023~~and ~~; May 29 ~~/05 to~~ to Jul 01~~/07/~~, 2024). These instances suggest that in conditions of increasing surface roughness on a wet snow surface, additional source of uncertainty in S1 retrievals from field data might be associated to the IEM ~~modeling~~ (see Sec. 3.2) translating surface roughness in ~~backscattering~~ backscatter response and/or to point-wise panel measurements underestimating the surface roughness of the entire S1 cell. In ~~this sense, the fact that the chosen reference cell might slightly overlap with the snow surface disturbed by snow profile digging is another factor to consider to explain discrepancies between S1 recordings and retrievals. In Fig. 12~~ Tab. 3 we labeled these sources as "~~uncertainties in IEM modeling~~uncertainty in IEM modelling" and "~~uncertainties in~~ uncertainty in surface roughness measurements", respectively.

Interestingly, the S1 signal saturates ~~on both years~~ at values of σ_0^{VV} ~~around ~-20 dB , which is~~ of -22.4 and -23.7 dB for 2023 and 2024, respectively. These values are close to the nominal noise equivalent sigma naught (NESZ) of S1, i.e. -22 dB. The saturation of the signal is obtained by SMRT at much lower values, around ~-30 dB, regardless of the chosen permittivity ~~model~~formulation.

4.3.1 C-band radar ~~backscattering~~ backscatter sensitivity to the coupled evolution of surface roughness and liquid water content

To study the C-band radar ~~backscattering~~ backscatter sensitivity to the coupled evolution of surface roughness and LWC, we selected the date of Apr 16~~/04/~~, 2024. On this date, we measured a melt event in the superficial 45 cm. The bottom part of the snowpack was homogeneously dry and was discretized as a one layer with the average of the scattering properties measured in the field. These values are representative of a compacted snowpack structure at the beginning of the melt process: density of 428 kgm^{-3}, SSA of 15.1 m^{2}kg^{-1} and temperature of -0.1~~°~~°C. From this configuration, we prepared a series of synthetic

snowpack variations with surface LWC increasing from 0 to 12%, and coupled each of them with a range of surface roughness RMSH increasing from 1 to 15 mm. ~~The extremes of the explored surface roughness range~~ These extremes represent a smooth surface ~~characteristic~~ typical of recent snowfall and the highly textured surface of fully formed suncups, respectively. To ensure consistency, we gradually increased the value of the second roughness parameter CL as well. To do so, we used an empirical logarithmic relationship extracted from field data between RMSH and CL, which we report in Fig. A1. However, this empirical relationship is based on a limited number of points (75 in total) which show larger ~~spreads~~ spread for increasing values of RMSH. Therefore, we assume that the only ~~discontinuity in the experiment~~ two discontinuities in the experimental results (see Fig. 14~~b, $RMSH =$~~a-c, RMSH=3 mm and ~~$LWC_{top} =$~~$LWC_{top} =$12%) can be explained considering this uncertainty. ~~We run all experiments with the same incidence angle of 41°~~For clarity, these points were removed. All experiments were run with two incidence angles – 30° and 40° – which represent the overall range of angles between satellite overpasses and the snow surface within the reference cell (see Fig. 2 and Tab. 1). The result of all the experiments is shown in Fig. 14, for both permittivity formulations.

In general, Fig. 14 shows that the intensity of the scattering response has a strong dependence on LWC for lower values of surface roughness (~~$RMSH \leq$~~RMSH≤3 mm). The higher the surface roughness, the weaker the dependence on LWC. More in detail, with H-86, for LWC values lower or equal to 0.5%, simultaneously increasing surface LWC and surface roughness causes a decrease in C-band σ_0^{VV} of a maximum of 2 dB. Within this range, the intensity of the σ_0^{VV} drop from smooth to rough surfaces decreases gradually with increasing LWC. For LWC values higher than 0.5%, the spread in σ_0^{VV} as a function of increasing surface roughness for the same value of LWC increases, with a reversed trend. Simultaneously increasing LWC eventually generates a σ_0^{VV} increase for all the considered roughness values in this experiment. Interestingly, the higher the surface roughness, the lower LWC value is needed to invert the trend: for ~~$RMSH =$~~RMSH=15 mm (typical of a textured snow surface where suncups are visible, but also very close to the limit of validity of the IEM), σ_0^{VV} starts to increase for ~~$LWC \geq$~~LWC≥1%, whereas for ~~$RMSH =$~~RMSH=3 mm, the σ_0^{VV} only starts to increase for ~~$LWC \geq$~~LWC≥2%. For LWC values higher than the threshold of 0.5%, the surface roughness influences the C-band ~~backscattering~~ backscatter response to an extent that is comparable to the effect of LWC alone over a smooth surface. Similar considerations can be done for the experiments run with ~~the~~ MEMLSv3~~permittivity formulation~~, but as a consequence of the different absorption, the above-mentioned changes in σ_0^{VV} trends happen for lower values of LWC. ~~Besides these considerations~~Furthermore, the experiments in Fig. 14 reveal that, regardless of the permittivity formulation, for relatively low values of LWC (≃1%), a change in surface RMSH from 2 to 3 mm generates a remarkable ~~shift~~ increase of ≃6 dB in the ~~backscattering response. According to our field observations, such values were typically recorded~~ backscatter response. In our field campaign, we typically measured roughness values in this range over snow surfaces undergoing the first cycles of melt-refreeze metamorphism. Interestingly, the value of 6 dB is ~~almost exactly~~ very close to the average bias observed between S1 acquisitions and ~~modeled values of~~ SMRT-modelled σ_0^{VV} ~~with SMRT during the~~ during the moistening and ripening phase (see Tab. 4). ~~Therefore, we can conclude that the increase in backscattering from the minimum is due~~ This supports the hypothesis that panel measurements may underestimate the large-scale surface roughness. Moreover, the backscatter increase occurring for all LWC and regardless

of the incidence angle confirms that the monotonous increase in backscatter following the local minimum can be attributed to the formation of suncups, as initially suggested by the measurements alone.

Finally, Fig. 14c,f allow considerations regarding the impact of the incidence angle. To do so, we use the index $|\Delta\sigma_0^{VV}|_{40°-30°}$, i.e., the absolute difference in backscatter between the two incidence angles of 40° and 30° – the range of incidence angles overlooking the reference cell. For smooth surfaces ($1 \leq$RMSH≤ 2) and for LWC$\geq 1.5\%$, $|\Delta\sigma_0^{VV}|$ exceeds 2 dB, i.e., twice the nominal uncertainty of S1 (see Sec. 2.3). For LWC lower than 1.5%, $|\Delta\sigma_0^{VV}|$ is highly sensitive to small increases in LWC. For RMSH≥ 3, the sensitivity of $|\Delta\sigma_0^{VV}|$ to changes in LWC almost disappears. In conditions of fully-formed suncups (RMSH≥ 10), $|\Delta\sigma_0^{VV}|$ drops below the nominal sensitivity of 1.0 dB for every LWC value, meaning that the backscatter signals show progressively weaker angular dependence for highly structured snow surfaces. This phenomenon is easily understood considering that, on rough surfaces, diffuse scattering is enhanced. Therefore, the position of the sensor relatively to the snow surface becomes less important, as the reflected energy is less directional and more broadly scattered. The same phenomenon explains the apparent slight backscatter decrease for RMSH≥ 10 at angles of 30° (Fig. 14b,e). At lower incidence angles, the radar beam is closer to perpendicular to the surface than it is at higher incidence angles. On rough surfaces, with enhanced diffuse scattering, the fraction of energy reflected directly back to the sensor is reduced.

5 Discussion

Two consecutive years of detailed snow profiling with ~~a~~ specific focus on the melting season gave an unprecedented overview on the multitemporal evolution of the SAR ~~backscattering~~ backscatter as a result of the ~~measured~~ changing snowpack properties. The identification of the melting phases based on the ~~evolution of~~ multitemporal SAR backscattering as proposed by ~~(Marin et al., 2020)~~ Marin et al. (2020) was complicated by two factors: (i) the failure of Sentinel-1B in 2022, which resulted in a halved availability of satellite recordings and (ii) with the ideal incidence angle for wet snow separability being $\simeq$45° ~~(Karbou et al., 2021)~~(Nagler et al., 2016; Karbou et al., 2021), and as shown by the experiments in Fig. 14, lower incidence angles ~~likely dampened the backscattering response to wet~~ dampen the backscatter response to moistening snow. Despite these limitations, using nothing more than information on σ_0^{VV} change with respect to winter means, the threshold-based method identified the moistening and ripening phases for both years with high accuracy.

~~Using~~ With the first measured time series of surface roughness parameters, we demonstrated that for a high-altitude ~~Alpine snowpack ,~~ alpine snowpack – where radiation can be the dominant energy input during the melting season and surface roughness ~~normally~~ develops several weeks before the snow cover starts ~~forming patches ,~~ showing patches – the observed monotonous increase in ~~backscattering~~ backscatter at the end of the melting season is physically related to the development of surface roughness, from initial surface degradation due to melt-refreeze cycles and/or the sequence and intensity of snowfall events, to the formation of suncups. This ~~connection~~ phenomenon was only hypothesized by Marin et al. (2020)~~, as without ground data~~. Without ground truth reference, it is impossible to distinguish the effect of surface roughness from ~~patchy~~ disappearing snow using multitemporal SAR ~~backscattering~~ backscatter alone. Additionally, the start of the monotonous increase in multitemporal SAR ~~backscattering~~ backscatter defines the local minima in the time series. Several studies were

carried out in recent years where such minima were associated to the runoff start (Gagliano et al., 2023; Darychuk et al., 2023). However, the proximity of backscatter minimum and runoff start is not due to SAR direct detection of meltwater. Instead, this apparent coincidence arises at the specific frequency of S1 because of an interplay of several factors. As the snowpack reaches the maximum detectable water content by S1 (which reduces scattering), surface roughness begins to develop, enhancing scattering. These mechanisms will be discussed individually in the remaining of this discussion. Based on our data, the only and most likely conclusion we can ~~extrapolate from the backscattering~~ draw from the backscatter minima from a practical point of view is that the snowpack is in an isothermal state and likely *already* releasing water. However, processes such as melt-refreeze cycles, sublimation, compaction, or settlement in the upper snow layers can potentially lead to the formation of rough surfaces before the snowpack starts releasing meltwater runoff. Therefore, it is relevant to rethink how information on ~~backscattering~~ backscatter minima are used for hydrological applications, especially when counting on a limited satellite revisit frequency. Further research should also investigate other potential energy input mechanisms that are typical of snowpacks in environments outside the high-altitude and mid-latitude conditions explored in this study.

~~Reproducing satellite backscattering through radiative transfer modeling driven by field measurements involves~~ With radiative transfer modelling, we were able to link measured snow properties to retrieved satellite-based radar signals, aiming at reproducing the multitemporal backscatter time series recorded by S1. This analysis revealed that – rather than melting phases – the multitemporal S1 backscatter time series identify two main regimes, each driven by a different dominant factor influencing the radar response: LWC and surface roughness. Thus, as shown in Fig. 12, the moistening and ripening phases could be merged into a single phase primarily dominated by LWC, whereas the runoff phase could be redefined as a roughness-dominated phase. Modelling satellite backscatter signals forced by field measurements requires accounting for several sources of uncertainty, which ~~can be categorized into two main factors: LWC and surface roughness~~are predominantly associated to these two variables. The uncertainty associated to LWC manifests itself in many different ways: the time lag between satellite and measurement acquisitions, the scattering originating from surface structures formed by melt-refreeze cycles, the spatial heterogeneity of the LWC distribution, the instrument uncertainty associated to the measurements and, ~~more~~ on the RT ~~modeling~~ modelling side, a lack of a definite permittivity formulation for wet snow. The uncertainty associated to surface roughness is mostly linked to measurement inaccuracies (and/or not representativeness for the entire S1 cell) and, on the RT ~~modeling~~ modelling side, to possible errors in the IEM surface model.

Within the approximately 5 hours separating satellite and measurements acquisitions, the liquid water per layer can change significantly (Kendra et al., 1998; Techel and Pielmeier, 2011), especially during the moistening and ripening phases or within cold spells, as indicated by the higher simulation variabilities in Fig. 12. ~~Especially on~~ On early stages of the melt process, our measurements are likely not representative ~~for~~ of the snowpack state overlooked by S1 because of the strong effect of melt-refreeze. Our findings confirm that C-band σ_0^{VV} is highly sensitive to diurnal snowpack variability, particularly during the early stages of melting when features such as melt-refreeze crusts are present (Lund et al., 2022; Brangers et al., 2024). As noted in Brangers et al. (2024), this strong dependence potentially complicates LWC retrievals significantly at these latitudes. This point raises concerns, because the early stages of melting represent a critical period when S1 can detect LWC and likely the only window of opportunity to obtain and integrate reasonable information. However, our RT simulations forced by field

measurements were able to attribute the observed σ_0^{VV} drops across all tracks over both years – 6.2, 4.2, 1.5, and 7.8 dB – to corresponding measured TWC of 3, 1, 2, and 34 mm, respectively. These results are in line with the tower-based experiments of Strozzi et al. (1997); Strozzi and Matzler (1998).

Another issue is the instrument uncertainty in LWC measurements. The deviations between dielectric and calorimetric measurements that we obtained throughout the campaign are in line with previous field and lab studies (Kinar and Pomeroy, 2015; Avanzi et al., 2016). Unexpectedly, co-located measurements in 2023 in the presence of ice lenses showed smaller deviations with respect to simultaneous measurements in 2024. Localized high values of LWC, such as for ponding meltwater above ice lenses, can pose accuracy problems for instruments that empirically estimate the volumetric liquid water content from the snow permittivity (Techel and Pielmeier, 2011). However, as already discussed, their presence could homogenize the overall liquid water distribution among the cell overlooked by the satellite. The increased variability between measurement techniques in 2024 may be (at least partially) due to the increased LWC hetereogeneity compared to 2023. This may indicate that the snowpack stratigraphy and LWC conditions play a larger role than measurement errors due to spatial and temporal offsets. Accounting for the LWC instrument uncertainty ~~,~~ which we estimated ~~to approximately 1% from our data and which are~~ being approximately 1% from our measurements, and in line with previous similar comparative studies (Techel and Pielmeier, 2011; Donahue et al., 2022) ~~,~~ generates an uncertainty range in the simulated σ_0^{VV} which is higher than the variability of the ~~satellite recorded σ_0^{VV}~~ signal recorded by S1 over the course of one snow season. Highest deviations happen for highest values of LWC, in ~~accordance~~ line with the findings of Veyssière et al. (2019).

Finally, the lack of a definitive permittivity formulation for wet snow poses a significant challenge for the scientific community. ~~Developing~~ The permittivity formulations selected for this study exhibit similar spectral shapes (see Fig. 5) and are, to our knowledge, the only ones that have been validated against real-world observations at C-band frequencies. As mentioned in Sec. 3.2, the permittivity formulation describes how the real and imaginary part of ϵ_s change with increasing fractions of liquid water, and therefore how radar microwaves interact with the snowpack. ϵ_s is computed using mixing theories to account for volume fractions of ice, water and air in the snow medium. MEMLSv3 parametrizes the shape of water inclusions as elongated spheroids embedded in a homogeneous host medium. This represents an important source of uncertainty. As liquid water increases, the shape and orientation of water inclusions significantly affects ϵ_s, as the electromagnetic field interacts with them in a shape-dependent way, generating anisotropic responses (Arslan et al., 2003; Chang et al., 2016). However, characterizing the temporal evolution of the shape of water inclusions during melting processes is an ambitious and challenging task that has only been addressed very recently by Krol et al. (2024) through rapid MRI profiling in a controlled laboratory environment. At the time our measurement campaign was designed and conducted, these methods did not yet exist – let alone their applicability in the field, which is still entirely unknown. These recent advancements are highly promising for the crucial challenge of developing a comprehensive model applicable across all frequencies and LWC conditions~~is crucial. This study highlights the discrepancies between simulated and actual S1 backscattering measurements, possibly due to overestimated absorption loss in existing models~~ . ~~While matching the observed backscattering would suggest an imaginary permittivity~~ Moreover, Fig. 12 highlights discrepancies of approximately 6 dB between SMRT-simulated and satellite-recorded backscatter signals, especially when σ_0^{VV} is largely dominated by LWC. Similar deviations were found by Veyssière et al. (2019) using MEMLS&a

to reproduce σ_0^{VV} during consecutive melt seasons over alpine areas. Additionally, both permittivity models saturate σ_0^{VV} at values below -30 dB. Such low values are never recorded by S1, which saturates at around -22 dB. Similar signal saturation (between -20 and -25 dB) in the C-band in vertical co-polarizations are confirmed by the tower-based radiometric studies of Strozzi et al. (1997); Strozzi and Matzler (1998). Matching the recorded S1 σ_0^{VV} would require an imaginary part of ϵ_s similar to that at 1 GHz ~~,~~ this would imply unrealistic penetration depths ~~at~~ for the C-band, contradicting field observations (Ulaby and Herschel Stiles, 1981; Shi and Dozier, 1995; Ulaby et al., 2014; Lodigiani et al., 2025). ~~Despite this uncertainty, utilizing two different models derived from distinct mixing theories, yet exhibiting similar spectral shapes (see Fig. 5), allowed for an evaluation of the impact of various uncertainty sources and scattering mechanisms. However, the inherent limitations in~~ We conclude that one possible explanation to the observed deviations is the overestimated absorption loss in the existing permittivity formulations. In view of the described inherent limitations of existing wet snow permittivity ~~models prevented~~ formulations, a detailed quantitative analysis of ~~individual scattering contributions . This~~ scattering contributions from individual snow layers was not possible. As previously noted in Sec. 3.2, the absence of a unified permittivity model for wet snow remains an important ~~area~~ direction for future research – not only for RT modelling, but also for field measurements, since dielectric methods depend on such models to derive LWC.

Later in the melting season, the effects of the uncertainties associated to LWC become weaker, because the snowpack surface becomes wetter and the scattering is mostly dominated by surface effects (Shi and Dozier, 1992) – this can be observed in Fig. 12~~on dates where the variabilities~~ , as variability associated to LWC ~~decrease gradually as a function of time. On these stages~~decreases gradually with time. Simultaneously, deviations between ~~radiative transfer simulations and satellite acquisitions~~ modelled and recorded σ_0^{VV} decrease sensibly (groups 3-4a and 4-5b in Fig. 12). Here, deviations are mostly explained by ~~inaccuracies in surface roughness measurements~~inaccurate surface roughness quantification. This is ~~clearly demonstrated by cases where there is a notable loss of simulation accuracy following~~ particularly evident on instances where simulation accuracy drops after a spring snowfall ~~, after surface roughness~~ on a surface that had already begun ~~to develop~~ developing marked roughness (see "buried surface roughness" instances in Fig. 12). However, at these later stages of the melting process, simulations reproduce the recorded ~~backscattering~~ backscatter generally well. ~~Further~~ This is confirmed by the low RMSE values reported in Tab. 4 for the runoff phase, which we redefined as a phase dominated by surface roughness effects. Here, further deviations can be attributed to ~~the possibility that the panel measurements may not fully capture the roughness~~ panel measurements possibly not capturing fully the large-scale roughness features observed by the satellite. This hypothesis seems to be confirmed by the very recent results of Barella et al. (2025), which show that panel sizes practical for field measurements may be insufficient to capture the roughness features of wider areas. Additionally, the IEM model, which translates roughness parameters into scattering, could be affected by inaccuracies, ~~particularly~~ especially when the roughness ~~is high enough to approach the limits of~~ values approach or exceed the model's ~~validity (see Fig. 3.2)~~range of validity.

In other words, with Fig. 12, we tried to reproduce the recorded S1 σ_0^{VV} over a 20 × 20 m cell using ~~physically based~~ physics-based averages of fine, detailed snow properties measured at the point scale. At wider scales, the relative importance of very specific information on the state of the snowpack may decrease compared to more influential large-scale scattering drivers, namely the development of internal snowpack structures (e.g. ice lenses and crusts), the soil features in the case of an isothermal

but predominantly dry snowpack, and large-scale surface roughness. Although the modularity and comprehensiveness of SMRT theoretically allows most of these scenarios to be ~~modeled~~modelled, the problem of how to quantify them on a large scale persists.

In Fig. 14, we selected a realistic snowpack layering observed in the field and used the full range of measured values of surface roughness to repeat the experiments done in the past by ~~Shi and Dozier (1992)~~ Shi and Dozier (1992); Strozzi et al. (1997); Strozzi and Matzler (1998). These simulations aimed to characterize the scattering response ~~to increasing surface roughness on~~ of a wet snow cover to increasing surface roughness, while varying the incidence angle to match the range observed across the relative S1 orbits covering the study area. Since the relationship between co-polarized signals and snow wetness is controlled by the scattering mechanisms, the type of correlation between superficial LWC and surface roughness expresses the relative contribution of volume rather than surface scattering mechanisms (Shi and Dozier, 1992). Shi and Dozier (1992) found negative correlations with surface roughness for LWC between 2 and 4% and a positive correlation with increasing surface wetness at an incidence angle of 50~~°~~°. Similar results were also found by Ulaby and Herschel Stiles (1981) at frequencies of 8.6 GHz and incidence angles greater than 50~~°~~°. Our results generally confirm these findings, but the wider range of explored combinations of surface roughness and LWC reveals that the correlation tilt does not occur at a specific LWC value. For RMSH values (simply "roughness" hereafter) between 2 and 10 mm, typical of snow during most of the melting period, the tilt depends on both LWC and ~~RMSH~~roughness, shifting towards higher LWC with lower ~~RMSH~~roughness. Specifically, ~~backscattering~~ backscatter strongly depends on LWC when ~~$RMSH \leq$~~roughness values exceed 3 mm. ~~For low RMSH values (1–2~~ Again, for smooth surfaces (1-2 mm), both permittivity models saturate σ_0^{VV} below -30 dB, a value never recorded by S1~~, even in multi-year time series, where saturation occurs around -20 dB~~.

An interesting ~~finding~~ result from Fig. 12 is that the most accurate simulations of S1 recordings happen ~~with~~ when measured values of surface ~~RMSH above or equal~~ roughness equal or exceed the threshold value of 3 mm. The experimental analyses in Fig. 14 ~~shows~~ show that, for relative low values of LWC between 1 and 1.5%, the ~~backscattering~~ backscatter response increases by approximately 6 dB when the roughness ~~RMSH~~ increases from 2 to 3 mm. The value of 6 dB is almost exactly the bias we observed in Fig. 12 between S1 recordings and our simulations, especially with increasing LWC. ~~Similar~~ As mentioned, similar deviations were found by Veyssière et al. (2019)~~using MEMLS&a to reproduce σ_0^{VV} during consecutive melt seasons over Alpine areas~~. Additionally, for LWC values $\geq$1.5% and ~~RMSH~~ roughness between 3 and 4 mm, the simulated σ_0^{VV} saturates at values that are comparable to those recorded by S1. This raises the point that more representative estimates of surface roughness for the entire S1 cell, and/or improved IEM ~~modeling~~ modelling to translate this information into ~~backscattering~~ backscatter signals, could be just as crucial as rigorous permittivity formulations for accurately reproducing and better interpreting multitemporal S1 σ_0^{VV}. ~~Finally~~Recent findings by Barella et al. (2025) also point to this direction, suggesting that commonly used transect extraction algorithms may filter out some small-scale roughness features. In general, the experiments in Fig. 14 represent a substantial advancement with respect to Shi and Dozier (1992); Strozzi et al. (1997); Strozzi and Matzler (1998). In these earlier experiments, surface roughness was either not quantitatively measured (being only qualitatively assessed), and/or evaluated over a very limited set of scenarios, overlooking intermediate conditions that, as our measurements prove, characterize the majority of the melting period.

Fig. 14c,f show that for smooth surfaces and for LWC values as low as 1.5% – i.e., when the melting process is likely in its initial stage – the variation in backscatter across the range of incidence angles overlooking the reference cell is comparable to or even exceeds the threshold used in Nagler and Rott (2000); Nagler et al. (2016); Marin et al. (2020) for wet snow detection. This angular dependence constitutes an additional uncertainty factor in wet snow detection, which overlaps with the previously discussed effects of diurnal variability in snowpack properties. On the other hand, for LWC values higher than 2% on smooth surfaces, the angular dependence increases up to 3 dB. This result supports the hypothesis that two distinct scattering mechanisms observed across the two seasons are directly linked to incidence angle effects. The first is a persistent 3–5 dB difference in σ_0^{VV} between the two ascending tracks, recorded from mid-April to early June 2023 (see Fig. 8a). This spread was not observed in the following year. Our LWC measurements indicate that the snowpack surface was wetter in 2023 than in 2024, likely due to the presence of ice lenses acting as drainage barriers for meltwater and favoring the formation of a wetter layer above them (see Fig. 13 and Tab. 5). Consequently, and in line with the results in Fig. 14, the smoother and wetter snow surface in 2023 led to a stronger angular dependence compared to 2024. Additionally, the angular dependence decreases with increasing surface roughness. The second observed feature is the sharp decrease in backscatter between consecutive acquisitions of both ascending and descending tracks in 2024 — from June 15 to 22 and from June 19 to 26, respectively. Our measurements indicate conditions of high snowpack saturation and surface roughness values equal to or exceeding 10 mm (see Fig. 13 and Tab. 5). Consistent with the results shown in Fig. 14b,e, we interpret this decrease as the result of suncups formation on a saturated snow surface. The enhanced surface roughness likely increased diffuse scattering and reduced the proportion of energy reflected back to the sensor, thereby explaining the observed backscatter decrease. These findings indicate that, despite all the aforementioned challenges in deriving LWC from backscatter and vice versa, the multitemporal analysis of angular dependence may carry valuable additional information. Unfortunately, further analysis in this direction was limited by the reduced revisit frequency of S1 during the period of this study.

Ultimately, Fig. 14 suggests that with an estimate of the surface LWC from a detailed snow model and recorded values of S1 ~~backscattering~~backscatter, it is in principle possible to give an estimate of the surface roughness. This would inform on two interesting points. On the one hand, based on the position with respect to the curve tilt, it would be possible to have information about the dominance of the volume versus surface scattering mechanism. A prevalence of volume scattering would mean that the snowpack has not yet become a complete black body for C-band radar ~~backscattering~~backscatter. On the other hand, the value of surface roughness could be assimilated in ~~physically based~~ physics-based snow models to estimate important metrics for the computation of turbulent heat fluxes, such as the aerodynamic roughness length (Lehning et al., 2011).

Although promising for future research, this paper comes with a number of limitations. LWC is a key variable for interpreting and reproducing S1 acquisitions using radiative transfer models. However, despite ongoing advancements, accurately measuring LWC in the field, ~~modeling it within physically based~~ modelling it within physics-based snow models, and accounting for it into permittivity models remain significant challenges which need to be solved individually. The halved availability of satellite data acquisitions due to the failure of Sentinel-1B in the exact time span when this study was carried out hindered the possibility to obtain more information than those presented on the relationship between melting ~~processes~~ snowpack properties and the multitemporal SAR ~~backscattering~~backscatter. Finally, despite this study enhanced significantly the understanding of

the interaction of SAR ~~backscattering~~ backscatter with wet snow, these findings are likely valid for ~~high-Alpine~~ high-alpine regions, i.e. homogeneously covered by a rather high amount of snow, and where surface roughness can develop before the snow cover disappears in patches. However, the launch of the Sentinel-1C satellite will shortly restore the mission's full capabilities~~, providing enhanced data availability~~. This development will hopefully spark greater interest in the field, driving research efforts to address the above mentioned limitations, explore ~~mechanisms in environments outside~~ scattering mechanisms in other environments than the one explored in this study, and potentially establish a new role for radiative transfer ~~modeling~~ modelling – specifically, to inform ~~physically-based~~ physics-based snow models for hydrological applications.

6 Conclusions

In this paper, we presented a unique dataset of wet snow scattering properties collected at a high vertical and temporal resolution over two snow seasons at the ~~high-Alpine~~ high-alpine field site of Weissfluhjoch, Davos, Switzerland. Using this dataset, we analyzed the correlation between melting snow properties and multitemporal SAR ~~backscattering~~ backscatter from S1, and ~~reproduced the acquired~~ modelled the satellite signals using the radiative-transfer model SMRT. Our data show that the moistening and the ripening phase, being mostly related to the presence of liquid water in the snowpack, are generally well ~~recognized~~ identified using time series of multitemporal SAR ~~backscattering~~ backscatter from S1. The runoff onset, often associated with local minima in multitemporal SAR ~~backscattering~~backscatter, is not detectable by the satellite. With our measurements, we showed that these local minima result from a combination of surface wetting, which reduces ~~backscattering~~ backscatter until the S1 signal saturates, and the development of surface roughness before the snow cover begins to disappear in patches, leading to an increase in ~~backscattering~~backscatter. Therefore, it is important to rethink how this information is used for hydrological applications at high elevations and mid-latitudes, especially when counting on reduced satellite revisit times, like in this study. Then, we used our dataset as input to the SMRT model to reproduce the S1 ~~backscattering~~ backscatter signal. The simulations ~~were generally affected by~~ generally showed a negative bias with respect to ~~the satellite data~~satellite acquisitions, with the most significant drivers being LWC in earlier stages of the ~~melt~~ melting process and the surface roughness later on. ~~Furthermore, we highlighted key difficulties in electromagnetic modeling~~ This mismatch led to the insight that, rather than melting phases, the multitemporal S1 backscatter time series reveal two dominant scattering regimes: one dominated by LWC and the other by surface roughness. These two regimes also represent the main sources of uncertainty in electromagnetic modelling of melting snowpacks~~based on field measurements~~. These challenges include ~~uncertainties primarily deriving from~~ the spatial and temporal variability of LWC between field measurements and satellite ~~acquisitions~~overpasses, inaccuracies in surface roughness ~~measurements, and the validity of~~ estimation, and limitations in the permittivity and roughness models ~~for wet snow at~~ applicable to wet snow in the C-band. Despite these uncertainties, radiative transfer ~~modeling forced~~ modelling driven by ground measurements allowed in-depth physical ~~interpretations~~ interpretation of scattering mechanisms at different ~~melting~~ stages. Specifically, the unprecedented time series of measured surface roughness parameters ~~made it possible to explore and define~~ allowed exploring and defining the scattering effect of roughness over wetting snowpacks. Our findings suggest that accurately quantifying surface roughness and/or improving the transfer function in IEM ~~modeling~~ modelling could

be as critical as developing new, rigorous permittivity formulations to enhance S1 retrievals and ~~enhance~~ the understanding of scattering mechanisms on wet snow at these wavelengths. With improved process understanding, the imminent restoration of the ~~the Sentinel~~ S1 mission full capabilities, and further validation efforts in radiative transfer sub-modules, the use of C-band satellite radar signals for snow hydrology applications could proceed further, with radiative transfer models possibly informing ~~physically based~~ physics-based snow models.

Code and data availability. The code to reproduce the simulations and plot of Fig. 12 is available on GitHub (https://github.com/carlettif/multitemporal-s1-backscattering). The SMRT model code is available on GitHub (https://github.com/smrt-model/smrt/releases/tag/v1.1). The manually measured and automatically recorded data used in this paper are available on Envidat (https://doi.org/10.16904/envidat.574). All Sentinel-1 data is freely available at https://dataspace.copernicus.eu/ upon registration.

Author contributions. FC: conceptualization, data acquisition, data curation, methodology, formal analysis, investigation, visualization, writing (original draft, review and editing). CM: conceptualization, data acquisition, methodology, project administration, funding acquisition, writing (review and editing). CG: data acquisition, data curation, writing (review and editing). MB: conceptualization, data acquisition, project administration, funding acquisition, writing (review and editing). ML: conceptualization, project administration, funding acquisition, writing (review and editing).

Competing interests. The authors declare that they have no competing interests.

Acknowledgements. This research was funded by the Swiss National Science Foundation, grant number 20021-205190. The authors acknowledge all the project partners and employees who took part in the measurement campaign and the contributors to the development of the SMRT model.

References

Achammer, T. and Denoth, A.: Snow dielectric properties: from DC to microwave X-band, Annals of Glaciology, 19, 92–96, https://doi.org/10.3189/S0260305500011034, 1994.

Anttila, K., Manninen, T., Karjalainen, T., Lahtinen, P., Riihelä, A., and Siljamo, N.: The temporal and spatial variability in submeter scale surface roughness of seasonal snow in Sodankylä Finnish Lapland in 2009–2010, Journal of Geophysical Research: Atmospheres, 119, 9236–9252, https://doi.org/https://doi.org/10.1002/2014JD021597, 2014.

Arslan, A., Wang, H., Pulliainen, J., and Hallikainen, M.: Scattering from wet snow by applying strong fluctuation theory, Journal of Electromagnetic Waves and Applications, 17, 1009–1024, https://doi.org/10.1163/156939303322519081, 2003.

Avanzi, F., Hirashima, H., Yamaguchi, S., Katsushima, T., and De Michele, C.: Observations of capillary barriers and preferential flow in layered snow during cold laboratory experiments, The Cryosphere, 10, 2013–2026, https://doi.org/10.5194/tc-10-2013-2016, 2016.

Barella, R., Marin, C., Mattia, C., Gianinetto, M., Moranduzzo, T., and Notarnicola, C.: A Low-Cost Portable Automatic System for Snow Surface Roughness Measurements Based on Digital Photography, in: 2021 IEEE International Geoscience and Remote Sensing Symposium IGARSS, pp. 5562–5565, https://doi.org/10.1109/IGARSS47720.2021.9553989, 2021.

Barella, R., Bavay, M., Carletti, F., Ciapponi, N., Premier, V., and Marin, C.: Unlocking the potential of melting calorimetry: a field protocol for liquid water content measurement in snow, The Cryosphere, 18, 5323–5345, https://doi.org/10.5194/tc-18-5323-2024, 2024.

Barella, R., Bavay, M., Carletti, F., Mazza, A., Scheidt, K. T., Walter, B., and Marin, C.: Characterizing Snow Roughness: A Novel Low-Cost Portable Tool Based on Charuco Board and Digital Photography, SSRN Electronic Journal, https://doi.org/10.2139/ssrn.5333224, preprint, 2025.

Bartelt, P. and Lehning, M.: A physical SNOWPACK model for the Swiss avalanche warning: Part I: numerical model, Cold Regions Science and Technology, 35, 123–145, https://doi.org/https://doi.org/10.1016/S0165-232X(02)00074-5, 2002.

Bellaire, S., van Herwijnen, A., Mitterer, C., and Schweizer, J.: On forecasting wet-snow avalanche activity using simulated snow cover data, Cold Regions Science and Technology, 144, 28–38, https://doi.org/https://doi.org/10.1016/j.coldregions.2017.09.013, international Snow Science Workshop 2016 Breckenridge, 2017.

Beniston, M. and Stoffel, M.: Rain-on-snow events, floods and climate change in the Alps: Events may increase with warming up to 4°C and decrease thereafter, Science of The Total Environment, 571, 228–236, https://doi.org/https://doi.org/10.1016/j.scitotenv.2016.07.146, 2016.

Beniston, M., Farinotti, D., Stoffel, M., Andreassen, L. M., Coppola, E., Eckert, N., Fantini, A., Giacona, F., Hauck, C., Huss, M., Huwald, H., Lehning, M., López-Moreno, J.-I., Magnusson, J., Marty, C., Morán-Tejéda, E., Morin, S., Naaim, M., Provenzale, A., Rabatel, A., Six, D., Stötter, J., Strasser, U., Terzago, S., and Vincent, C.: The European mountain cryosphere: a review of its current state, trends, and future challenges, The Cryosphere, 12, 759–794, https://doi.org/10.5194/tc-12-759-2018, 2018.

Benninga, H.-J. F., van der Velde, R., and Su, Z.: Sentinel-1 soil moisture content and its uncertainty over sparsely vegetated fields, Journal of Hydrology X, 9, 100 066, https://doi.org/https://doi.org/10.1016/j.hydroa.2020.100066, 2020.

Brangers, I., Marshall, H.-P., De Lannoy, G., Dunmire, D., Mätzler, C., and Lievens, H.: Tower-based C-band radar measurements of an alpine snowpack, The Cryosphere, 18, 3177–3193, https://doi.org/10.5194/tc-18-3177-2024, 2024.

Brogioni, M., Pettinato, S., Macelloni, G., Paloscia, S., Pampaloni, P., Pierdicca, N., and Ticconi, F.: Sensitivity of bistatic scattering to soil moisture and surface roughness of bare soils, International Journal of Remote Sensing, 31, 4227–4255, https://doi.org/10.1080/01431160903232808, 2010.

Chang, W., Ding, K.-H., Tsang, L., and Xu, X.: Microwave Scattering and Medium Characterization for Terrestrial Snow With QCA–Mie and Bicontinuous Models: Comparison Studies, IEEE Transactions on Geoscience and Remote Sensing, 54, 3637–3648, https://doi.org/10.1109/TGRS.2016.2522438, 2016.

Conger, S. M. and McClung, D. M.: Comparison of density cutters for snow profile observations, Journal of Glaciology, 55, 163–169, https://doi.org/10.3189/002214309788609038, 2009.

Copernicus: Copernicus data hub, https://scihub.copernicus.eu/.

Darychuk, S. E., Shea, J. M., Menounos, B., Chesnokova, A., Jost, G., and Weber, F.: Snowmelt characterization from optical and synthetic-aperture radar observations in the La Joie Basin, British Columbia, The Cryosphere, 17, 1457–1473, https://doi.org/10.5194/tc-17-1457-2023, 2023.

Denoth, A.: Snow dielectric measurements, Advances in Space Research, 9, 233–243, https://doi.org/https://doi.org/10.1016/0273-1177(89)90491-2, 1989.

Denoth, A.: An electronic device for long-term snow wetness recording, Annals of Glaciology, 19, 104–106, https://doi.org/10.3189/S0260305500011058, 1994.

Denoth, A., Foglar, A., Weiland, P., Mätzler, C., Aebischer, H., Tiuri, M., and Sihvola, A.: A comparative study of instruments for measuring the liquid water content of snow, Journal of Applied Physics, 56, 2154–2160, https://doi.org/10.1063/1.334215, 1984.

Dingman, S.: Physical Hydrology, Waveland Press, Incorporated, https://books.google.ch/books?id=hhWojwEACAAJ, 2015.

Donahue, C., Skiles, S. M., and Hammonds, K.: Mapping liquid water content in snow at the millimeter scale: an intercomparison of mixed-phase optical property models using hyperspectral imaging and in situ measurements, The Cryosphere, 16, 43–59, https://doi.org/10.5194/tc-16-43-2022, 2022.

Endrizzi, S., Gruber, S., Dall'Amico, M., and Rigon, R.: GEOtop 2.0: simulating the combined energy and water balance at and below the land surface accounting for soil freezing, snow cover and terrain effects, Geoscientific Model Development, 7, 2831–2857, https://doi.org/10.5194/gmd-7-2831-2014, 2014.

Fassnacht, S., Williams, M., and Corrao, M.: Changes in the surface roughness of snow from millimetre to metre scales, Ecological Complexity, 6, 221–229, https://doi.org/https://doi.org/10.1016/j.ecocom.2009.05.003, special Section: Fractal Modeling and Scaling in Natural Systems, 2009.

Fierz, C.: The International Classification for Seasonal Snow on the Ground, IHP-VI Technical Documents in hydrology, UNESCO/IHP, https://books.google.ch/books?id=1Su5ZwEACAAJ, 2009.

Fierz, C. and Föhn, P. M. B.: Long-Term Observation of the Water Content of an Alpine Snowpack, https://api.semanticscholar.org/CorpusID:127054238, 1994.

FPGA Company: SLF InfraSnow Sensor, https://fpga-company.com/wp-content/uploads/2023/01/InfraSnow-User-Manual-Version-1.01.pdf.

Fromm, R., Baumgärtner, S., Leitinger, G., Tasser, E., and Höller, P.: Determining the drivers for snow gliding, Natural Hazards and Earth System Sciences, 18, 1891–1903, https://doi.org/10.5194/nhess-18-1891-2018, 2018.

Fung, A., Li, Z., and Chen, K.: Backscattering from a randomly rough dielectric surface, IEEE Transactions on Geoscience and Remote Sensing, 30, 356–369, https://doi.org/10.1109/36.134085, 1992.

Gagliano, E., Shean, D., Henderson, S., and Vanderwilt, S.: Capturing the Onset of Mountain Snowmelt Runoff Using Satellite Synthetic Aperture Radar, Geophysical Research Letters, 50, e2023GL105 303, https://doi.org/https://doi.org/10.1029/2023GL105303, e2023GL105303 2023GL105303, 2023.

Gergely, M., Wolfsperger, F., and Schneebeli, M.: Simulation and Validation of the InfraSnow: An Instrument to Measure Snow Optically Equivalent Grain Size, IEEE Transactions on Geoscience and Remote Sensing, 52, 4236–4247, https://doi.org/10.1109/TGRS.2013.2280502, 2014.

Günther, D., Marke, T., Essery, R., and Strasser, U.: Uncertainties in Snowpack Simulations—Assessing the Impact of Model Structure, Parameter Choice, and Forcing Data Error on Point-Scale Energy Balance Snow Model Performance, Water Resources Research, 55, 2779–2800, https://doi.org/https://doi.org/10.1029/2018WR023403, 2019.

Hallikainen, M., Ulaby, F., and Abdelrazik, M.: Dielectric properties of snow in the 3 to 37 GHz range, IEEE Transactions on Antennas and Propagation, 34, 1329–1340, https://doi.org/10.1109/TAP.1986.1143757, 1986.

HannaInstrumentsInc.: HI98501 (Checktemp®) Instruction Manual, Hanna Instruments.

Husman, S. d. R., Hu, Z., Wouters, B., Munneke, P. K., Veldhuijsen, S., and Lhermitte, S.: Remote Sensing of Surface Melt on Antarctica: Opportunities and Challenges, IEEE Journal of Selected Topics in Applied Earth Observations and Remote Sensing, 16, 2462–2480, https://doi.org/10.1109/JSTARS.2022.3216953, 2023.

Karbou, F., Veyssière, G., Coleou, C., Dufour, A., Gouttevin, I., Durand, P., Gascoin, S., and Grizonnet, M.: Monitoring Wet Snow Over an Alpine Region Using Sentinel-1 Observations, Remote Sensing, 13, https://doi.org/10.3390/rs13030381, 2021.

Kattelmann, R. and Dozier, J.: Observations of snowpack ripening in the Sierra Nevada, California, U.S.A., Journal of Glaciology, 45, 409–416, https://doi.org/10.3189/S002214300000126X, 1999.

Kawashima, K., Endo, T., and Takeuchi, Y.: A portable calorimeter for measuring liquid-water content of wet snow, Annals of Glaciology, 26, 103–106, https://doi.org/10.3189/1998AoG26-1-103-106, 1998.

Kendra, J., Sarabandi, K., and Ulaby, F.: Radar measurements of snow: Experiment and analysis, Geoscience and Remote Sensing, IEEE Transactions on, 36, 864 – 879, https://doi.org/10.1109/36.673679, 1998.

Kinar, N. J. and Pomeroy, J. W.: Measurement of the physical properties of the snowpack, Reviews of Geophysics, 53, 481–544, https://doi.org/https://doi.org/10.1002/2015RG000481, 2015.

Koch, F., Prasch, M., Schmid, L., Schweizer, J., and Mauser, W.: Measuring Snow Liquid Water Content with Low-Cost GPS Receivers, Sensors, 14, 20 975–20 999, https://doi.org/10.3390/s141120975, 2014.

Krol, Q., Scherrer, E., Skuntz, M., Codd, S., Hansen, A., and Seymour, J.: Rapid MRI profiling of liquid water content in snow: Melt and stability during first wetting and rain on snow events, in: Proceedings of the International Snow Science Workshop, Montana State University Library, Tromsø, Norway, https://arc.lib.montana.edu/snow-science/objects/ISSW2024_O3.11.pdf, 2024.

Leduc-Leballeur, M., Picard, G., Mialon, A., Arnaud, L., Lefebvre, E., Possenti, P., and Kerr, Y.: Modeling L-Band Brightness Temperature at Dome C in Antarctica and Comparison With SMOS Observations, IEEE Transactions on Geoscience and Remote Sensing, 53, 4022–4032, https://doi.org/10.1109/TGRS.2015.2388790, 2015.

Lehning, M., Völksch, I., Gustafsson, D., Nguyen, T. A., Stähli, M., and Zappa, M.: ALPINE3D: a detailed model of mountain surface processes and its application to snow hydrology, Hydrological Processes, 20, 2111–2128, https://doi.org/https://doi.org/10.1002/hyp.6204, 2006.

Lehning, M., Grünewald, T., and Schirmer, M.: Mountain snow distribution governed by an altitudinal gradient and terrain roughness, Geophysical Research Letters, 38, https://doi.org/https://doi.org/10.1029/2011GL048927, 2011.

Lin, C.-C., Rommen, B., Floury, N., Schüttemeyer, D., Davidson, M. W. J., Kern, M., Kontu, A., Lemmetyinen, J., Pulliainen, J., Wiesmann, A., Werner, C. L., Mätzler, C., Schneebeli, M., Proksch, M., and Nagler, T.: Active Microwave Scattering Signature of Snow-

pack—Continuous Multiyear SnowScat Observation Experiments, IEEE Journal of Selected Topics in Applied Earth Observations and Remote Sensing, 9, 3849–3869, https://doi.org/10.1109/JSTARS.2016.2560168, 2016.

Lodigiani, M., Marin, C., and Pasian, M.: Mixed Analytical-Numerical Modeling of Radar Backscattering for Seasonal Snowpacks, IEEE Journal of Selected Topics in Applied Earth Observations and Remote Sensing, 18, 3461–3471, https://doi.org/10.1109/JSTARS.2024.3521612, 2025.

Lombardo, M., Fees, A., Udke, A., Meusburger, K., van Herwijnen, A., Schweizer, J., and Lehmann, P.: Capillary suction across the soil-snow interface as a mechanism for the formation of wet basal layers under gliding snowpacks, Journal of Glaciology, p. 1–46, https://doi.org/10.1017/jog.2025.2, 2025.

Lund, J., Forster, R. R., Deeb, E. J., Liston, G. E., Skiles, S. M., and Marshall, H.-P.: Interpreting Sentinel-1 SAR Backscatter Signals of Snowpack Surface Melt/Freeze, Warming, and Ripening, through Field Measurements and Physically-Based SnowModel, Remote Sensing, 14, https://doi.org/10.3390/rs14164002, 2022.

Lundberg, A., G. N. G. D.: "Ground Trut" snow measurements – review of operational and new measurement methods for Sweden, Norway, and Finland, pp. 215–237, 2008.

Magagi, R. and Bernier, M.: Optimal conditions for wet snow detection using RADARSAT SAR data, Remote Sensing of Environment, 84, 221–233, https://doi.org/https://doi.org/10.1016/S0034-4257(02)00104-9, 2003.

Manninen, T., Anttila, K., Karjalainen, T., and Lahtinen, P.: Automatic snow surface roughness estimation using digital photos, Journal of Glaciology, 58, 993–1007, https://doi.org/10.3189/2012JoG11J144, 2012.

Marin, C., Bertoldi, G., Premier, V., Callegari, M., Brida, C., Hürkamp, K., Tschiersch, J., Zebisch, M., and Notarnicola, C.: Use of Sentinel-1 radar observations to evaluate snowmelt dynamics in alpine regions, The Cryosphere, 14, 935–956, https://doi.org/10.5194/tc-14-935-2020, 2020.

Marty, C. and Meister, R.: Long-term snow and weather observations at Weissfluhjoch and its relation to other high-altitude observatories in the Alps, Theoretical and Applied Climatology, 110, https://doi.org/10.1007/s00704-012-0584-3, 2012.

Meloche, J., Langlois, A., Rutter, N., Royer, A., King, J., Walker, B., Marsh, P., and Wilcox, E. J.: Characterizing tundra snow sub-pixel variability to improve brightness temperature estimation in satellite SWE retrievals, The Cryosphere, 16, 87–101, https://doi.org/10.5194/tc-16-87-2022, 2022.

Meloche, J., Leroux, N. R., Montpetit, B., Vionnet, V., and Derksen, C.: Radar Equivalent Snowpack: reducing the number of snow layers while retaining its microwave properties and bulk snow mass, EGUsphere, 2024, 1–18, https://doi.org/10.5194/egusphere-2024-3169, 2024.

Miranda, N., Meadows, P., Hajduch, G., Pilgrim, A., Piantanida, R., Giudici, D., Small, D., Schubert, A., Husson, R., Vincent, P., Mouche, A., Johnsen, H., and Palumbo, G.: The Sentinel-1A instrument and operational product performance status, in: 2015 IEEE International Geoscience and Remote Sensing Symposium (IGARSS), pp. 2824–2827, https://doi.org/10.1109/IGARSS.2015.7326402, 2015.

Mitchell, K. A. and Tiedje, T.: Growth and fluctuations of suncups on alpine snowpacks, Journal of Geophysical Research: Earth Surface, 115, https://doi.org/https://doi.org/10.1029/2010JF001724, 2010.

Moldestad, D. A.: Characterisation of liquid water content and snow density in a cross-country race ski track, Bulletin of glaciological research, 22, 39–49, 2005.

Murfitt, J., Duguay, C., Picard, G., and Lemmetyinen, J.: Forward modelling of synthetic-aperture radar (SAR) backscatter during lake ice melt conditions using the Snow Microwave Radiative Transfer (SMRT) model, The Cryosphere, 18, 869–888, https://doi.org/10.5194/tc-18-869-2024, 2024.

Mätzler, C.: Applications of the interaction of microwaves with the natural snow cover, Remote Sensing Reviews, 2, 259–387, https://doi.org/10.1080/02757258709532086, 1987.

Naderpour, R., Schwank, M., Houtz, D., Werner, C., and Mätzler, C.: Wideband Backscattering From Alpine Snow Cover: A Full-Season Study, IEEE Transactions on Geoscience and Remote Sensing, 60, 1–15, https://doi.org/10.1109/TGRS.2021.3112772, 2022.

Nagler, T. and Rott, H.: Retrieval of wet snow by means of multitemporal SAR data, IEEE Transactions on Geoscience and Remote Sensing, 38, 754–765, https://doi.org/10.1109/36.842004, 2000.

Nagler, T., Rott, H., Ripper, E., Bippus, G., and Hetzenecker, M.: Advancements for Snowmelt Monitoring by Means of Sentinel-1 SAR, Remote Sensing, 8, https://doi.org/10.3390/rs8040348, 2016.

Perla, R. and Banner, J.: Calibration of capacitive cells for measuring water in snow, Cold Regions Science and Technology, 15, 225–231, https://doi.org/https://doi.org/10.1016/0165-232X(88)90069-9, 1988.

Pfeffer, W. T. and Humphrey, N. F.: Formation of ice layers by infiltration and refreezing of meltwater, Annals of Glaciology, 26, 83–91, https://doi.org/10.3189/1998AoG26-1-83-91, 1998.

Picard, G., Sandells, M., and Löwe, H.: SMRT: an active–passive microwave radiative transfer model for snow with multiple microstructure and scattering formulations (v1.0), Geoscientific Model Development, 11, 2763–2788, https://doi.org/10.5194/gmd-11-2763-2018, 2018.

Picard, G., Leduc-Leballeur, M., Banwell, A. F., Brucker, L., and Macelloni, G.: The sensitivity of satellite microwave observations to liquid water in the Antarctic snowpack, The Cryosphere, 16, 5061–5083, https://doi.org/10.5194/tc-16-5061-2022, 2022a.

Picard, G., Löwe, H., and Mätzler, C.: Brief communication: A continuous formulation of microwave scattering from fresh snow to bubbly ice from first principles, The Cryosphere, 16, 3861–3866, https://doi.org/10.5194/tc-16-3861-2022, 2022b.

Picard, G., Löwe, H., Domine, F., Arnaud, L., Larue, F., Favier, V., Le Meur, E., Lefebvre, E., Savarino, J., and Royer, A.: The Microwave Snow Grain Size: A New Concept to Predict Satellite Observations Over Snow-Covered Regions, AGU Advances, 3, e2021AV000 630, https://doi.org/https://doi.org/10.1029/2021AV000630, e2021AV000630 2021AV000630, 2022c.

Porod, G.: Die Röntgenkleinwinkelstreuung von dichtgepackten kolloiden Systemen, Kolloid-Zeitschrift, 124, 83–114, https://doi.org/10.1007/BF01512792, 1951.

Post, A. and LaChapelle, E. R.: Glacier ice, University of Toronto Press, 2000.

Proksch, M., Mätzler, C., Wiesmann, A., Lemmetyinen, J., Schwank, M., Löwe, H., and Schneebeli, M.: MEMLS3a: Microwave Emission Model of Layered Snowpacks adapted to include backscattering, Geoscientific Model Development, 8, 2611–2626, https://doi.org/10.5194/gmd-8-2611-2015, 2015.

Proksch, M., Rutter, N., Fierz, C., and Schneebeli, M.: Intercomparison of snow density measurements: bias, precision, and vertical resolution, The Cryosphere, 10, 371–384, https://doi.org/10.5194/tc-10-371-2016, 2016.

Quegan, S. and Yu, J. J.: Filtering of multichannel SAR images, IEEE Transactions on Geoscience and Remote Sensing, 39, 2373–2379, https://doi.org/10.1109/36.964973, 2001.

Quéno, L., Vionnet, V., Cabot, F., Vrécourt, D., and Dombrowski-Etchevers, I.: Forecasting and modelling ice layer formation on the snowpack due to freezing precipitation in the Pyrenees, Cold Regions Science and Technology, 146, 19–31, https://doi.org/https://doi.org/10.1016/j.coldregions.2017.11.007, 2018.

Raleigh, M. S., Lundquist, J. D., and Clark, M. P.: Exploring the impact of forcing error characteristics on physically based snow simulations within a global sensitivity analysis framework, Hydrology and Earth System Sciences, 19, 3153–3179, https://doi.org/10.5194/hess-19-3153-2015, 2015.

Rott, H., Scheiblauer, S., Wuite, J., Krieger, L., Floricioiu, D., Rizzoli, P., Libert, L., and Nagler, T.: Penetration of interferometric radar signals in Antarctic snow, The Cryosphere, 15, 4399–4419, https://doi.org/10.5194/tc-15-4399-2021, 2021.

Sandells, M., Löwe, H., Picard, G., Dumont, M., Essery, R., Floury, N., Kontu, A., Lemmetyinen, J., Maslanka, W., Morin, S., Wiesmann, A., and Mätzler, C.: X-Ray Tomography-Based Microstructure Representation in the Snow Microwave Radiative Transfer Model, IEEE Transactions on Geoscience and Remote Sensing, 60, 1–15, https://doi.org/10.1109/TGRS.2021.3086412, 2022.

Schmid, L., Heilig, A., Mitterer, C., Schweizer, J., Maurer, H., Okorn, R., and Eisen, O.: Continuous snowpack monitoring using upward-looking ground-penetrating radar technology, Journal of Glaciology, 60, 509–525, https://doi.org/10.3189/2014JoG13J084, 2014.

Schwerdt, M., Schmidt, K., Tous Ramon, N., Klenk, P., Yague-Martinez, N., Prats-Iraola, P., Zink, M., and Geudtner, D.: Independent System Calibration of Sentinel-1B, Remote Sensing, 9, 2017.

Shi, J. and Dozier, J.: Radar Backscattering Response to Wet Snow, in: [Proceedings] IGARSS '92 International Geoscience and Remote Sensing Symposium, vol. 2, pp. 927–929, https://doi.org/10.1109/IGARSS.1992.578299, 1992.

Shi, J. and Dozier, J.: Inferring snow wetness using C-band data from SIR-C's polarimetric synthetic aperture radar, IEEE Transactions on Geoscience and Remote Sensing, 33, 905–914, https://doi.org/10.1109/36.406676, 1995.

Shi, J., Dozier, J., and Rott, H.: Deriving snow liquid water content using C-band polarimetric SAR, in: Proceedings of IGARSS '93 - IEEE International Geoscience and Remote Sensing Symposium, pp. 1038–1041 vol.3, https://doi.org/10.1109/IGARSS.1993.322643, 1993.

Sihvola, A. H. and Tiuri, M. E.: Snow Fork for Field Determination of the Density and Wetness Profiles of a Snow Pack, IEEE Transactions on Geoscience and Remote Sensing, GE-24, 717–721, https://api.semanticscholar.org/CorpusID:10134466, 1986.

Smith, C. D., Kontu, A., Laffin, R., and Pomeroy, J. W.: An assessment of two automated snow water equivalent instruments during the WMO Solid Precipitation Intercomparison Experiment, The Cryosphere, 11, 101–116, https://doi.org/10.5194/tc-11-101-2017, 2017.

Soriot, C., Picard, G., Prigent, C., Frappart, F., and Domine, F.: Year-round sea ice and snow characterization from combined passive and active microwave observations and radiative transfer modeling, Remote Sensing of Environment, 278, 113 061, https://doi.org/https://doi.org/10.1016/j.rse.2022.113061, 2022.

Strozzi, T. and Matzler, C.: Backscattering measurements of alpine snowcovers at 5.3 and 35 GHz, IEEE Transactions on Geoscience and Remote Sensing, 36, 838–848, https://doi.org/10.1109/36.673677, 1998.

Strozzi, T., Wiesmann, A., and Mätzler, C.: Active microwave signatures of snow covers at 5.3 and 35 GHz, Radio Science, 32, 479–495, https://doi.org/10.1029/96RS03777, 1997.

Techel, F. and Pielmeier, C.: Point observations of liquid water content in wet snow ndash; investigating methodical, spatial and temporal aspects, The Cryosphere, 5, 405–418, https://doi.org/10.5194/tc-5-405-2011, 2011.

Torres, R., Snoeij, P., Geudtner, D., Bibby, D., Davidson, M., Attema, E., Potin, P., Rommen, B., Floury, N., Brown, M., Traver, I. N., Deghaye, P., Duesmann, B., Rosich, B., Miranda, N., Bruno, C., L'Abbate, M., Croci, R., Pietropaolo, A., Huchler, M., and Rostan, F.: GMES Sentinel-1 mission, Remote Sensing of Environment, 120, 9–24, https://doi.org/https://doi.org/10.1016/j.rse.2011.05.028, the Sentinel Missions - New Opportunities for Science, 2012.

Ulaby, F., Long, D., Blackwell, W., Elachi, C., Fung, A., Ruf, C., Sarabandi, K., Zyl, J., and Zebker, H.: Microwave Radar and Radiometric Remote Sensing, 2014.

Ulaby, F. T. and Herschel Stiles, W.: Microwave response of snow, Advances in Space Research, 1, 131–149, https://doi.org/https://doi.org/10.1016/0273-1177(81)90389-6, 1981.

Ulaby, F. T., Moore, R. K., and K., F. A.: Microwave Remote Sensing. Active and Passive. Vol. 3. From Theory to Applications, x + pp. 1065–2162. Norwood, MA: Artech House Inc. Price £79.00. ISBN 0 89006 192 0., Geological Magazine, 124, 88–88, https://doi.org/10.1017/S0016756800015831, 1987.

Veyssière, G., Karbou, F., Morin, S., Lafaysse, M., and Vionnet, V.: Evaluation of Sub-Kilometric Numerical Simulations of C-Band Radar Backscatter over the French Alps against Sentinel-1 Observations, Remote Sensing, 11, https://doi.org/10.3390/rs11010008, 2019.

Viviroli, D. and Weingartner, R.: The hydrological significance of mountains: from regional to global scale, Hydrology and Earth System Sciences, 8, 1017–1030, https://doi.org/10.5194/hess-8-1017-2004, 2004.

Wever, N., Würzer, S., Fierz, C., and Lehning, M.: Simulating ice layer formation under the presence of preferential flow in layered snowpacks, The Cryosphere, 10, 2731–2744, https://doi.org/10.5194/tc-10-2731-2016, 2016.

Wiesmann, A. and Mätzler, C.: Microwave Emission Model of Layered Snowpacks, Remote Sensing of Environment, 70, 307–316, https://doi.org/https://doi.org/10.1016/S0034-4257(99)00046-2, 1999.

Williams, L. D. and Gallagher, J. G.: The Relation of Millimeter-Wavelength Backscatter to Surface Snow Properties, IEEE Transactions on Geoscience and Remote Sensing, GE-25, 188–194, https://doi.org/10.1109/TGRS.1987.289817, 1987.

Wolfsperger, F., Ziegler, S., Schneebeli, M., and Löwe, H.: Evaluation of the InfraSnow: a handheld device to measure snow specific surface (SSA), https://doi.org/10.13140/RG.2.2.31566.95047, 2022.

Wolfsperger, F., Geisser, M., Ziegler, S., and Löwe, H.: A NEW HANDHELD CAPACITIVE SENSOR TO MEASURE SNOW DENSITY AND LIQUID WATER CONTENT, 2023.

Würzer, S., Jonas, T., Wever, N., and Lehning, M.: Influence of Initial Snowpack Properties on Runoff Formation during Rain-on-Snow Events, Journal of Hydrometeorology, 17, 1801 – 1815, https://doi.org/10.1175/JHM-D-15-0181.1, 2016.

Yueh, S. H., Dinardo, S. J., Akgiray, A., West, R., Cline, D. W., and Elder, K.: Airborne Ku-Band Polarimetric Radar Remote Sensing of Terrestrial Snow Cover, IEEE Transactions on Geoscience and Remote Sensing, 47, 3347–3364, https://doi.org/10.1109/TGRS.2009.2022945, 2009.

Zuanon, N.: IceCube, a portable and reliable instrument for snow specific surface area measurement in the field, https://api.semanticscholar.org/CorpusID:128982547, 2013.

Appendix A

~~Direct comparison of measured profiles of liquid water content with dielectric methods (brown) and melting calorimetry (blue). The uncertainty associated with melting calorimetry measurements as of Barella et al. (2021) is shown by means of the light blue shaded area. In 2024, a second profile using dielectric instruments (yellow) was simultaneously carried out alongside the melting calorimetry.~~

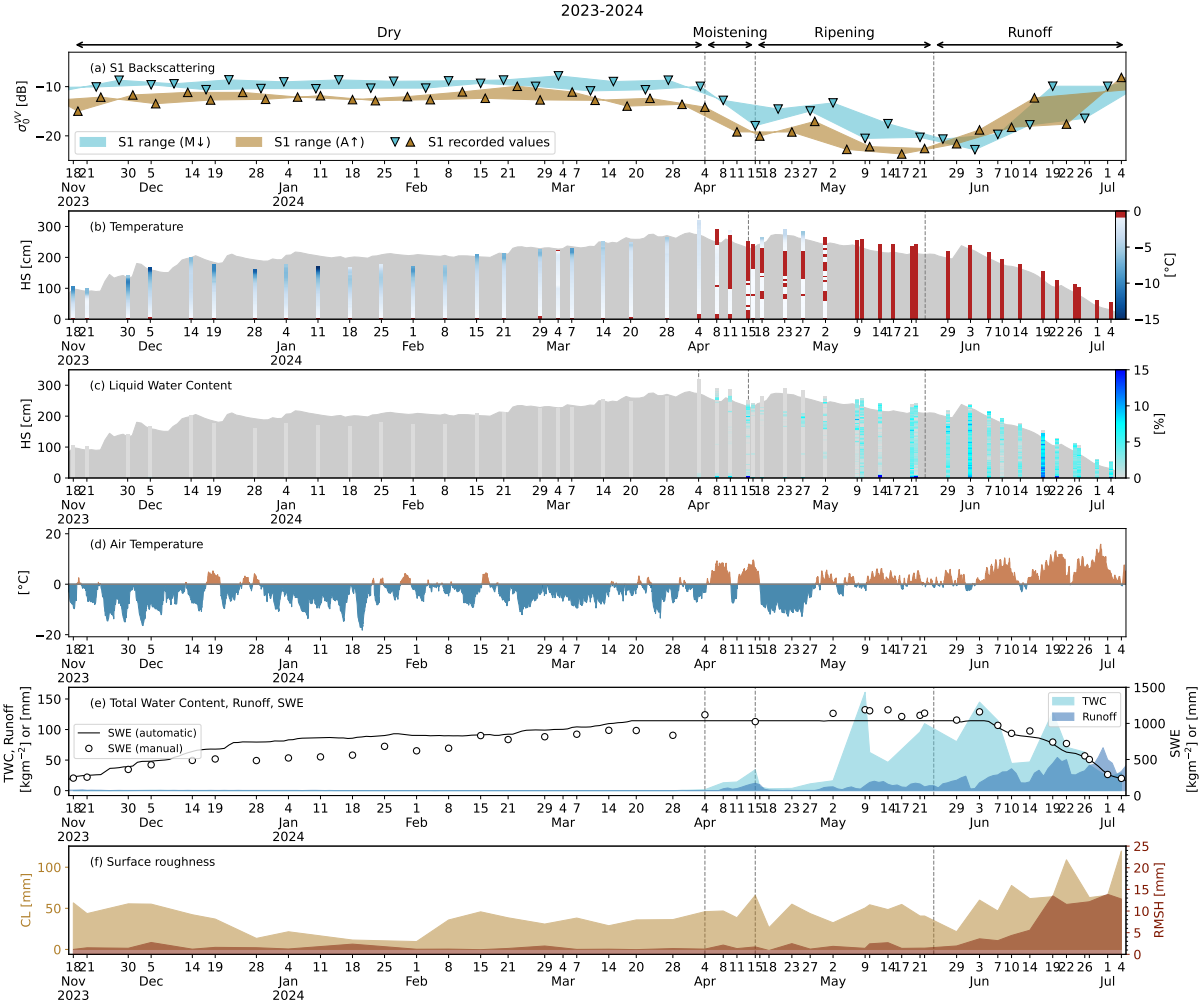

~~Data overview for the snow season of 2023-2024. Panel~~ (~~a~~b) ~~shows the manually~~ Manually measured ~~temperature~~ profiles of snow temperature. ~~Panel~~ (~~b~~c) ~~shows the manually~~ Manually measured ~~LWC~~ profiles of snow liquid water content (LWC). ~~Panel~~ (~~c~~d) ~~shows the air~~ Air temperature at hourly resolution~~as~~ , measured by the automatic sensor at WFJ. ~~Panel~~ (~~d~~e) ~~shows the measured~~ Measured total water content (TWC) (light blue)~~, the~~ ; runoff time series automatically recorded by the lysimeter at WFJ (dark blue)~~, the~~ ; snow water equivalent (SWE) both automatically recorded by the snow scale (black line) and manually measured (~~black points~~white circles). ~~Panel~~ (e) ~~shows the measured time~~ Time series of measured surface roughness ~~by means of the two indices~~ parameters – RMSH and CL.~~Panel (f) shows the recorded S1 time series divided into descending morning (light blue) and ascending afternoon (light brown) passages. In panel (f), the triangles indicate the exact values of S1 acquisitions, whereas shaded areas represent the range of σ_0^{VV} values obtained by connecting the consecutive S1 passages by direction of orbits, i.e. by connecting all the morning/descending and the afternoon/ascending acquisitions. Each panel is subdivided into the melting phases identified according to the method of Marin et al. (2020).~~

~~Data overview for the snow season of 2023-2024. Panel~~ (~~a~~b) ~~shows the manually~~ Manually measured ~~temperature~~ profiles of snow temperature. ~~Panel~~ (~~b~~c) ~~shows the manually~~ Manually measured ~~LWC~~ profiles of snow liquid water content (LWC). ~~Panel~~ (~~c~~d) ~~shows the air~~ Air temperature at hourly resolution~~as~~ , measured by the automatic sensor at WFJ. ~~Panel~~ (~~d~~e) ~~shows the measured~~ Measured total water content (TWC) (light blue)~~, the~~ ; runoff time series automatically recorded by the lysimeter at WFJ (dark blue)~~, the~~ ; snow water equivalent (SWE) both automatically recorded by the snow scale (black line) and manually measured (~~black points~~white circles). ~~Panel~~ (e) ~~shows the measured time~~ Time series of measured surface roughness ~~by~~

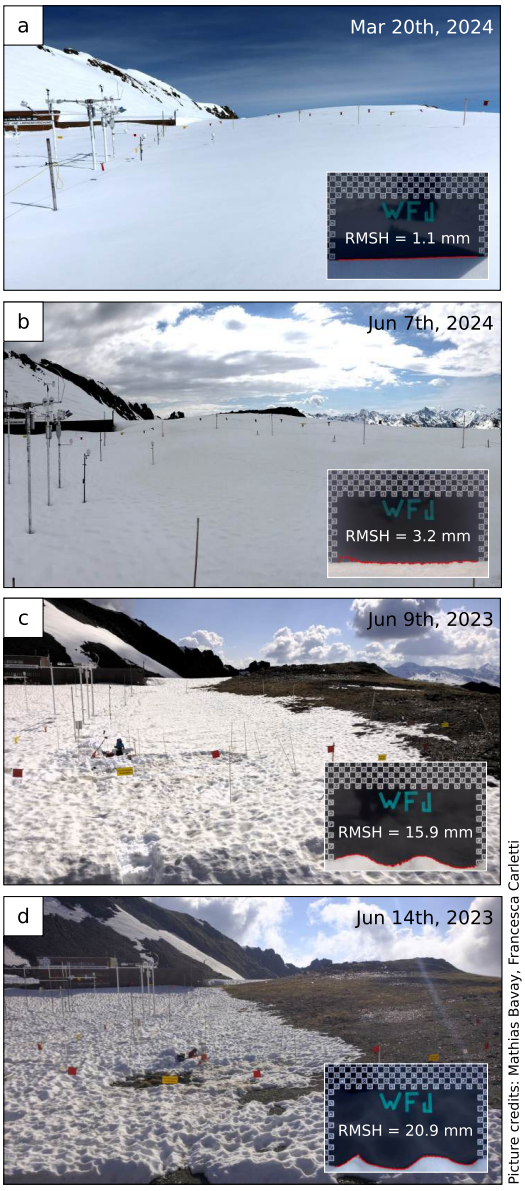

Figure 10. The panels illustrate some representative surface roughness conditions as qualitatively observed on the field (panoramic pictures) together with one of the panel measurements performed on the same day (bottom right of each panel, where the mean roughness RMSH measured on that day is also reported). ~~Panel~~ (a) ~~shows a smooth~~ Smooth surface typical of dry snowpack conditions. ~~Panel~~ (b) ~~shows early-stage~~ Early-stage development of surface roughness deriving from melt-refreeze cycles. ~~Panel~~ (c) ~~shows fully-formed~~ Fully-formed suncups over a homogeneous snow cover, at least among the considered S1 cell. ~~Panel~~ (d) ~~shows fully-formed~~ Fully-formed suncups over a ~~mostly~~ patchy snow cover.

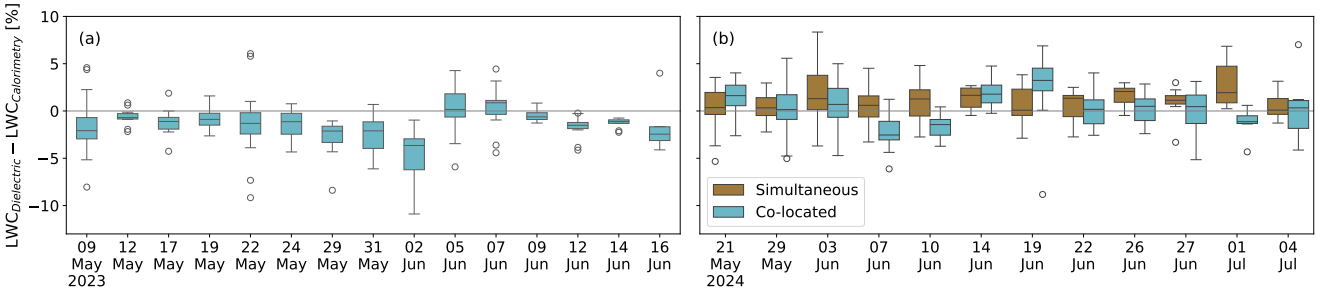

Figure 11. Bias between ~~liquid water content~~ LWC measurements with dielectric devices and melting calorimetry for snow seasons of 2023 (a) ~~2023~~ and 2024 (b)~~2024.~~. In 2024, direct comparisons between simultaneous (brown) and co-located (light blue) measurements ~~are available~~were also performed.

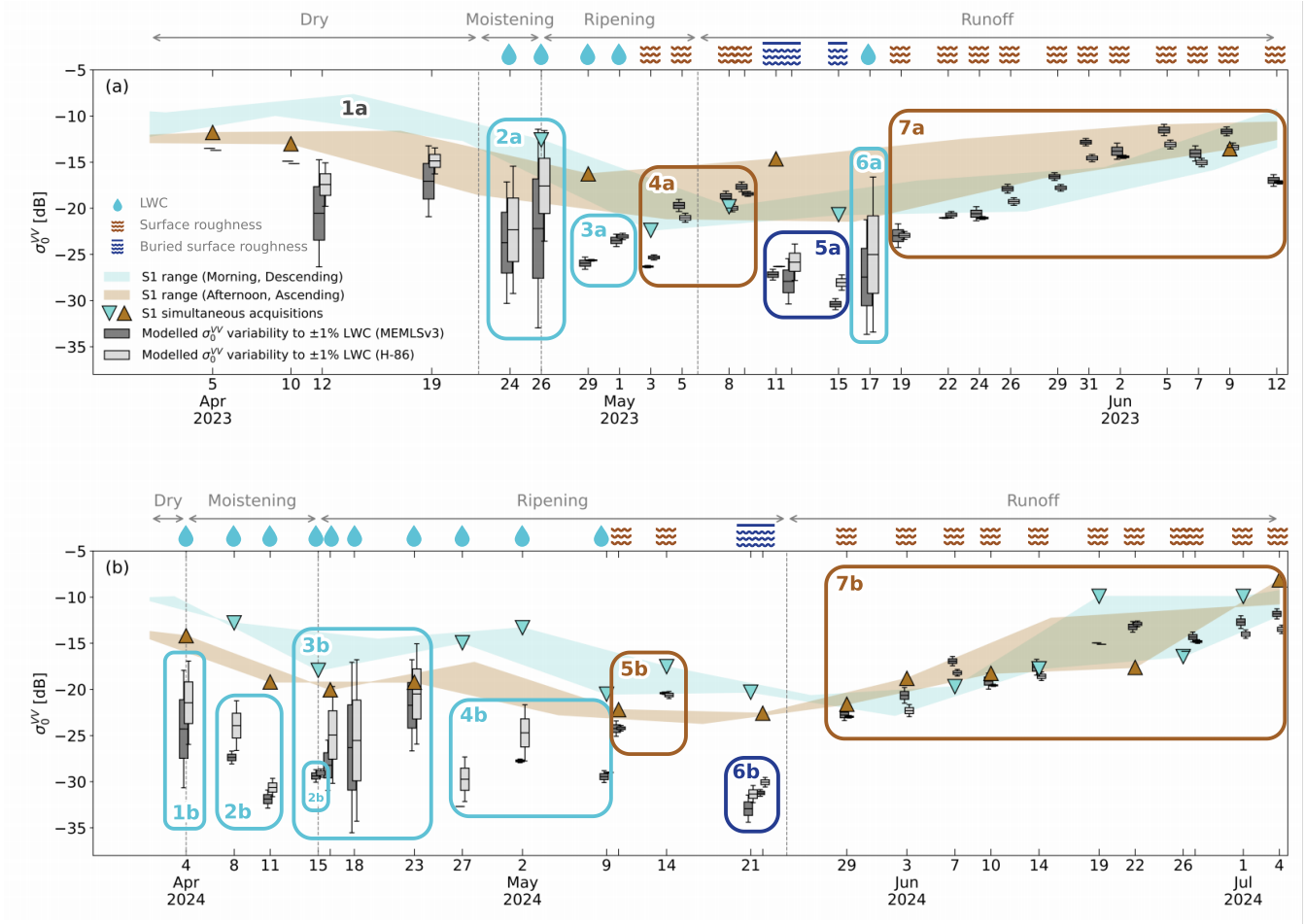

Figure 12. ~~Recorded S1~~ Comparison between the recorded multitemporal S1 σ_0^{VV} (~~light blue and light brown~~ triangles and shaded areas) ~~compared against SMRT modelled values~~ and the time series of σ_0^{VV} ~~using~~ modelled with SMRT, for year 2023 (a) and 2024 (b). Results are shown for both permittivity formulations – MEMLSv3 (dark gray boxplots) and H-86 (light gray boxplots)~~permittivity models~~. The boxplots indicate the variability ~~of~~ associated to the ~~results considering an~~ LWC uncertainty of ±1% ~~in the LWC values~~ for each layer~~(see~~, as discussed in Sec. 4.2~~)~~. The shaded areas of the recorded S1 multitemporal σ_0^{VV} represent the range of ~~σ_0^{VV}~~ values obtained by connecting the consecutive ~~S1~~ passages by direction of orbits, i.e. by connecting all the morning/descending and the afternoon/ascending acquisitions. The triangles represent the exact values of the acquisitions. For clarity, exact values are only shown for days where snow ~~profiles~~ measurements were carried out~~and therefore simulation and~~, thus allowing direct comparison~~is possible~~. ~~Blue~~ Colored boxes group similar simulation results ~~together~~and are labeled with codes (e.~~Yellow bold text indicates~~ g., 1a, 2a), which refer to Tab. 3 for details on the corresponding measured snow properties~~for each result group~~, ~~whereas blue italic text explains possible backscattering~~ dominant scattering mechanisms~~which may have originated~~, and potential sources of error. At the ~~(spread~~ top of ~~) simulated results~~each panel, the time series are further segmented into the melting phases identified in Sec. 4.1 – as well as the main scattering regimes, which are influenced by LWC, surface roughness, and buried surface roughness.

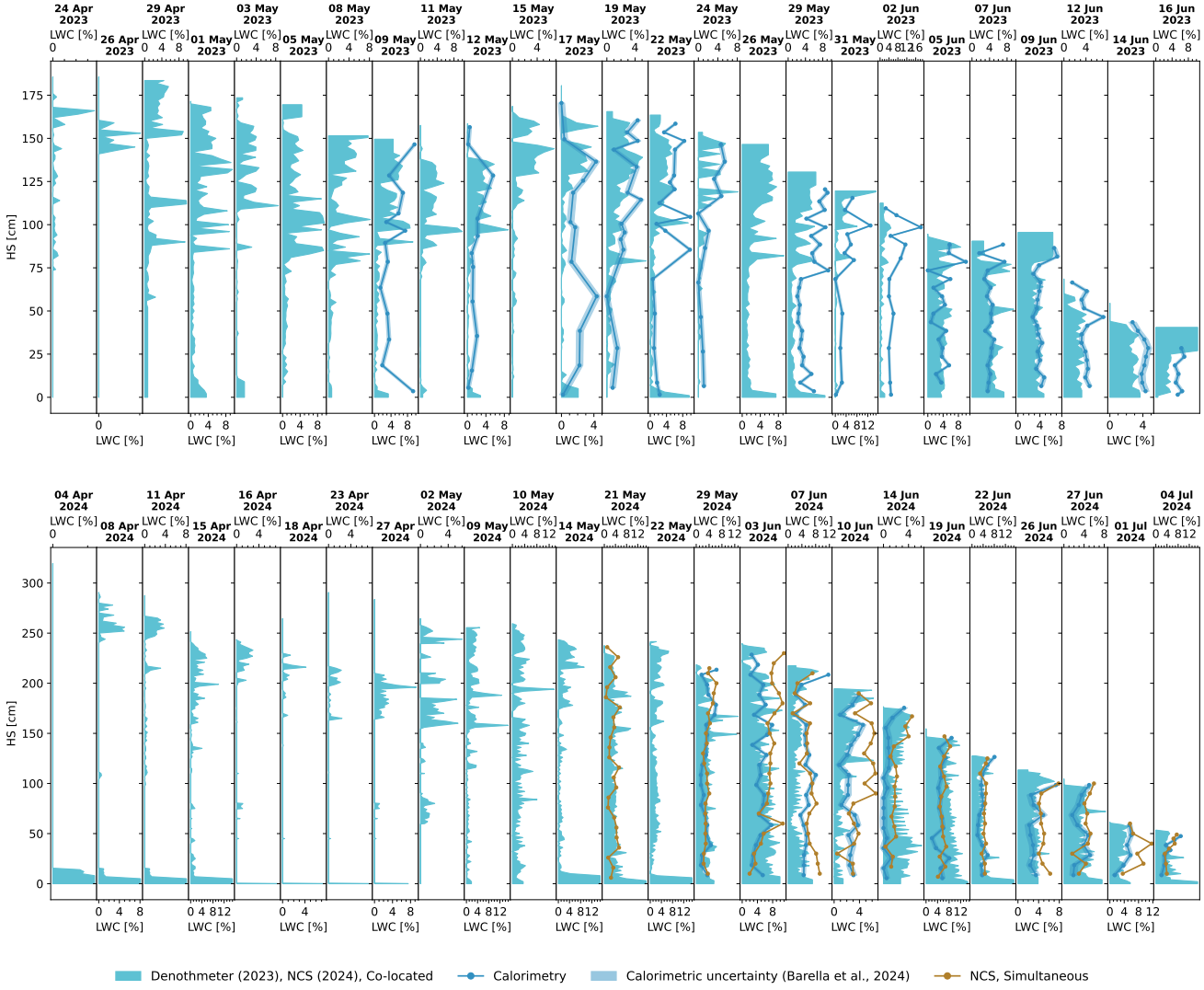

Figure 13. Ensemble of all the ~~measured~~ LWC profiles measured with dielectric instruments (light blue) from Apr 24~~/04/~~, 2023 and Apr 04~~/04/~~, 2024, i.e. the first dates for which ~~a~~ significant ~~discrepancies~~ mismatches between ~~modeled~~ modelled and S1-acquired σ_0^{VV} values ~~are recorded~~ in 2023 (top row) and 2024 (bottom row), respectively. Melting calorimetry measurements (~~see Fig~~dark blue), including their associated uncertainty (dark blue shaded areas) as described in Barella et al. (2024), are shown for comparison. ~~12~~In 2024, a second simultaneous LWC profile using dielectric instruments (brown) was also carried out.

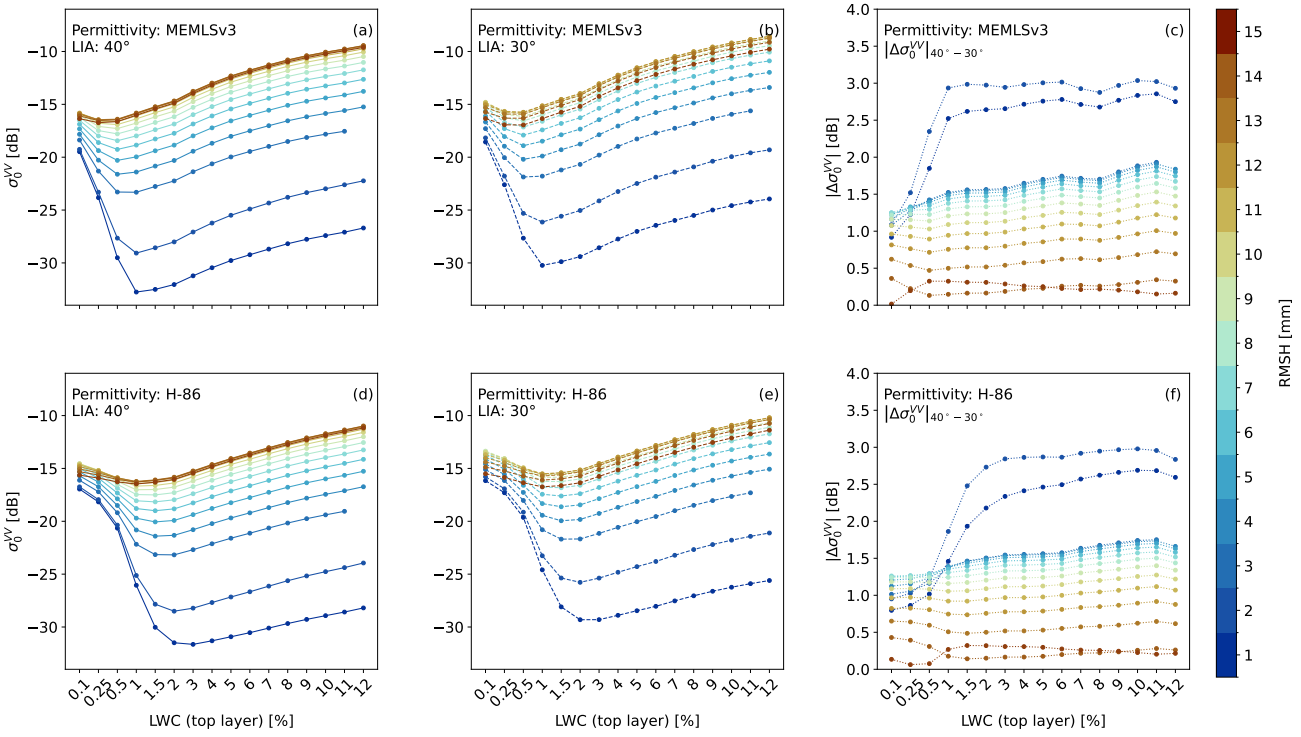

Figure 14. Sensitivity of the C-band radar ~~backscattering sensitivity~~ backscatter to the coupled evolution of surface roughness (expressed by RMSH) and LWC~~according to~~. Panels (a, b, d, e) illustrate differences between two dielectric permittivity formulations – MEMLSv3 (a, b) and H-86 (c, d) – as well as the sensitivity to the local incidence angle (LIA) over cell 40. σ_0^{VV} responses are shown for 40° (solid lines) and 30° (~~b~~dotted lines) ~~MEMLSv3 formulations~~incidence angles. ~~The top part~~ Panels (c, f) show values of ~~each panel shows~~ $|\Delta\sigma_0^{VV}|_{40°-30°}$, i.e., the ~~sensitivity of σ_0^{VV} to consecutive synthetic snowpack variations~~differences between backscatter coefficients in (a, b) and (d, e), respectively. The real reference case is the snowpack layering observed on Apr 16~~/04/~~, 2024: a melt event in the superficial 45 cm and an otherwise dry snowpack. The ~~bottom part of each panel shows the~~ reported results are consecutive ~~snowpack~~ synthetic variations ~~in terms~~ of ~~surface~~ LWC and roughness of the surface layer.

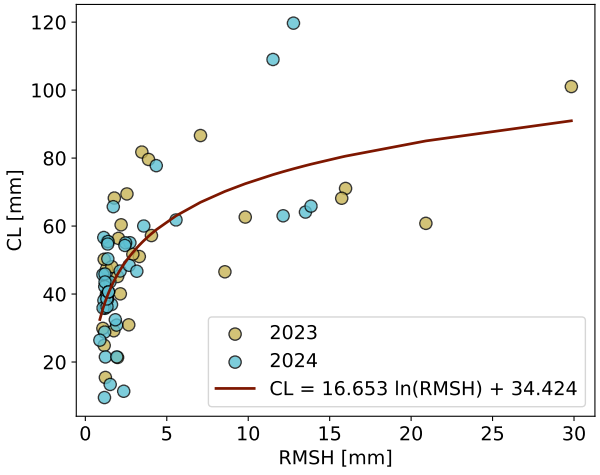

Figure A1. Empirical logarithmic relationship fitted on field data between the surface roughness parameters of RMSH and CL, based on a total of N=75 values over the measurement campaigns of 2023 (yellow) and 2024 (light blue).